

Image scaling by de la Vallée-Poussin filtered interpolation

Donatella Occorsio · Giuliana Ramella* · Woula Themistoclakis

Received: date / Accepted: date

Abstract We present a new image scaling method both for downscaling and upscaling, running with any scale factor or desired size. It is based on the sampling of an approximating bivariate polynomial, which globally interpolates the data and is defined by a filter of de la Vallée Poussin type whose action ray is suitable regulated to improve the approximation. The method has been tested on a significant number of different image datasets. The results are evaluated in qualitative and quantitative terms and compared with other available competitive methods. The perceived quality of the resulting scaled images is such that important details are preserved, and the appearance of artifacts is low. Very high-quality measure values in downscaling and the competitive ones in upscaling evidence the effectiveness of the method. Good visual quality, limited computational effort, and moderate memory demanding make the method suitable for real-world applications.

Keywords Image downscaling · Image upscaling · de la Vallée-Poussin Interpolation · Chebyshev nodes

Mathematics Subject Classification (2020) 94A08 · MSC 68U10 · 65D05 · 62H35

D. Occorsio
Department of Mathematics and Computer Science, University of Basilicata, Viale dell'Ateneo Lucano 10, 85100 Potenza, Italy E-mail: donatella.occorsio@unibas.it

G. Ramella (*corresponding author)
C.N.R. National Research Council of Italy, Institute for Applied Computations "Mauro Picone", Via P. Castellino, 111, 80131 Naples, Italy E-mail: giuliana.ramella@cnr.it

W. Themistoclakis
C.N.R. National Research Council of Italy, Institute for Applied Computations "Mauro Picone", Via P. Castellino, 111, 80131 Naples, Italy E-mail: woula.themistoclakis@cnr.it

1 Introduction

Image scaling aims to get the image at a different size preserving the original content as much as possible, with minor loss of quality, in two opposite ways: downscaling and upscaling. Downscaling is a compression process by which the size of the high-resolution (HR) input image is reduced to recover the low-resolution (LR) target image. Conversely, upscaling is an enhancement process in which the size of the LR input image is enlarged to regain the HR target image.

Image scaling (also termed image resampling or image resizing) is a widely used tool in several fields such as medical imaging, remote sensing, gaming, electronic publishing, autonomous driving, and aerial photography [2, 9, 22, 25, 31, 68]. For example, upscaling allows to highlight important details of the image in remote sensing and medical applications [2, 31], while downscaling is a fundamental operation for fast browsing or sharing purposes [9, 22]. Other applicative examples regard scenarios like deforestation, monitoring, traffic, surveillance, and many other engineering tasks. Sometimes image scaling is used for illicit purposes, e.g., to automatically generate camouflage images whose visual semantics change dramatically after scaling [63]. In these cases, it is very important to detect the scaling effects in order to defend against such attacks and adopt suitable countermeasures [5, 21].

From a computational point of view, image scaling can be addressed by different numerical methods (see Section 2) whose main critical points typically are: a) undesired effects, such as ringing artifacts and aliasing effect, due to the increase/decrease in the number of pixels which introduces/reduces information to the image; b) computational efficiency to perform the resampling task in the real-world applications. Moreover,

most of the existing methods treat the resampling in only one direction, being downscaling and upscaling often considered as separate problems in literature [10].

We aim to propose a scaling method that works in both downscaling and upscaling directions. To this aim, looking at the scaling problem as an approximation problem, we employ an interpolation polynomial based on an *adjustable* filter of de la Vallée Poussin type, which can be suitably modulated to improve the approximation (see, e.g. [39, 52, 55]).

Indeed, the de la Vallée-Poussin interpolation process has been introduced in literature as a valid alternative to Lagrange interpolation to provide a better pointwise approximation, especially when the Gibbs phenomenon occurs [37–39]. In fact, an interesting feature of de la Vallée Poussin filtered approximation is the presence of a free, additional degree-parameter which is responsible for the localization degree of the polynomial interpolation basis (the so-called fundamental de la Vallée Poussin polynomials) around the nodes. By changing this parameter, we may modulate the typical oscillatory behavior of the fundamental Lagrange polynomials in dependence on the data, improving the approximation without destroying the interpolation property but keeping fixed the number of the interpolation nodes. Moreover, it is also worth noting that de la Vallée Poussin interpolation can be embedded in a wavelet scheme with decomposition and reconstruction algorithms very fast since based on fast cosine transforms [7].

From a theoretical point of view, the literature concerning de la Vallée Poussin filtered approximation provides many convergence theorems, also in the uniform norm. They estimate an error comparable with the error of the best polynomial approximation [52, 53] and allow to predict the convergence order from the regularity of the function to approximate [36]. Due to such nice behavior, de la Vallée Poussin approximation has been usefully applied as a demonstration tool to carry out proofs of different theorems [12, 28, 29, 35, 54].

From a more applicative point of view, it has been used to solve singular integral and integro-differential equations [30], [11] or derive good quadrature rules for the finite Hilbert transform [40]. However, to our knowledge, it has never been applied to image processing. Hence, the present paper represents the first step in investigating how the de la Vallée-Poussin interpolation scheme can be usefully employed in image scaling.

To explain the proposed scaling method (shortly denoted by VPI), as a starting point, we consider that the input RGB image is represented at a continuous scale by a vectorial function (with separate channels for each color) whose sampling yields the pixels values. We

globally approximate such function using suitable de la Vallée Poussin interpolation polynomials [36–38, 52, 55]. Hence, we get the resized image by evaluating such de la Vallée Poussin polynomials in a denser (upscaling) or coarser (downscaling) grid of points.

The resulting VPI method achieves a good compromise between visual quality and processing time: the resized images present few blurred edges and artifacts, especially in downsampling, and the implementation is computationally simple and rather fast.

Being designed both for downscaling and upscaling, the VPI method is flexible and implementable for any scale factor. It does not require any input parameter, and the rescaling can be obtained by specifying the scale factor or, alternatively, the desired size of the image.

VPI method especially favors odd scale factors. In particular, using the same odd scale factor, we may sequentially run VPI first in upscaling (shortly u-VPI) and then in downscaling (shortly d-VPI), getting back the initial image without any error. More generally, we prove a theoretical estimate for d-VPI method that applied with any odd scale factor s produces an MSE not greater than s^2 times the MSE of the input data (cf. Proposition 1). Consequently, for any odd scale factor, we get a null MSE by applying d-VPI to an input image that is *exact* or, at least, only some *crucial* pixels of it are *exact* (cf. Remark 1).

A further contribution of this paper includes a detailed quantitative and qualitative analysis of the obtained results on several publicly available datasets commonly used in image processing. The experimental results confirm the effectiveness and utility of employing the de la Vallée-Poussin Interpolation scheme, achieving good quantitative results with an adequate balance. In general, we have a satisfactory performance, also for high scale factors, compared to other existing scaling methods. In particular, d-VPI has better performance than other downscaling methods achieving very high SSIM and PSNR values, while u-VPI has not such a superior performance as regards the other considered methods. Nevertheless, the quality metrics of u-VPI are in a competitive range and sometimes slightly better, with a limited computational effort and a moderate memory demanding.

Overall, due to its features, we consider VPI suitable for real-world applications, especially in downscaling. At the same time, we look at it as a complete method because it can also perform upscaling with adequate performance.

The organization of this paper is as follows. In Section 2, we outline the related work, briefly explaining the benchmark scaling methods in the experimen-

tal phase. In Section 3 we provide the mathematical background. In Section 4 we describe the VPI method and state its main properties. In Section 5 we provide the most relevant implementation details and the qualitative/quantitative evaluations of the experimental results taken over a large set of data. Finally, conclusions are drawn in Section 6.

2 Related work

Image scaling has received great attention in the literature of the past decades, during which many methods based on different approaches have been developed. An overview containing pros and cons for some of them can be found in [33, 66].

Traditionally, image scaling methods are grouped into two categories [43]: non-adaptive [4, 15, 26, 58, 64] and adaptive [1, 50, 51, 65, 69]. In the first category, all the pixels are equally treated. In the second, suitable changes are arranged, depending on image features and intensity values, edges information, texture, etc. Non adaptive category includes many of the most commonly used algorithms such as the nearest neighbor, bilinear, bicubic and B-splines interpolation, Lanczos method [4, 15, 26, 43, 58]. Adaptive methods are designed to maximize the quality of the results. They are also employed in most common approaches such as context-aware computing [51], segmentation techniques [50] and adaptive bilinear schemes [1]. Machine Learning (ML) methods can be ascribed to the latter category, even if they are often considered as a separate one [65, 69]. The learning paradigm of ML methods aims to compensate for complete (missing) information of the downsampled (upscaled) image using a relationship between HR (LR) and LR (HR) images. Mostly, this paradigm is implemented by a training step, in which the relationship is learned, followed by a step in which the learned knowledge is applied to unseen HR (LR) images.

Usually, non-adaptive scaling methods have problems of blurring or artifacts around edges and only store the low-frequency components of the original image. On the other hand, adaptive scaling methods generally provide better image visual quality and preserve high-frequency components. However, adaptive methods take more computational time as compared to non-adaptive ones. In turn, the ML methods ensure high-quality results but, at the same time, require extensive learning based on a huge number of parameters and labeled training images.

In this section we limit to describe shortly the methods considered in the validation phase of the VPI method (see Section 5), namely DPID [62], L_0 [23], SCN [60],

LCI [34] and BIC [18]. The source code of such methods is made available by the authors themselves in a common language (Matlab). Except for BIC and LCI, these methods are designed and tested considering the problem of resizing in one direction, i.e., in downscaling (DPID and L_0) or upscaling mode (SCN).

DPID is based on the assumption that Laplacian edge detector and adaptive low-pass filtering can be useful tools to approximate the behavior of the Human Visual System. Important details are preserved in the downsampled image by employing convolutional filters and by selecting the input pixels that contribute more to the output image the more their color deviates from their local neighborhood.

In L_0 , an optimization framework for image downscaling, focusing on two critical issues, is proposed: salient features preservation and downsampled image construction. Accordingly, two L_0 -regularized priors are introduced and applied iteratively until the objective function is verified. The first, based on gradient ratio, allows preserving the most salient edges and the visual perceptual properties of the original image. The second optimizes the downsampled image by the guidance of the original one, avoiding undesirable artifacts.

SCN (Sparse Coding based Network) adopts a neural network based on sparse coding, trained in a cascaded structure from end to end. It introduces some improvements in terms of both recovery accuracy and human perception employing a CNN (Convolutional Neural Network) model.

In LCI, the input RGB image is globally approximated by the bivariate Lagrange interpolating polynomial at a suitable grid of first kind Chebyshev zeros. The output RGB image is obtained by sampling this polynomial at the Chebyshev grid of the desired size.

BIC, one of the most commonly used rescaling methods, makes use of bicubic interpolation. It computes the unknown pixel value as a weighted average of 4×4 pixels closest to it. Note that BIC produces noticeably sharper images than the other classical non-adaptive methods as bilinear and nearest neighbor, offering w.r.t. them a favorable quality image and processing time ratio.

3 Mathematical preliminaries

Let I denote any color image of $n_1 \times n_2$ pixels, with $n_1, n_2 \in \mathbb{N}$. As is well-known, in the RGB space I is represented by means of a triad of $n_1 \times n_2$ matrices that we indicate using the same letter of the image they compose, namely I_k , with $k = 1 : 3$ (i.e. $k = 1, 2, 3$). The entries of these matrices are integers from 0 to \max_f that

denotes the maximum possible value of the image pixel, (e.g. $\max_f = 255$ if the pixels are represented using 8 bits per sample). On the other hand, such discrete values can be embedded in a vector function of the spatial coordinates, say $\mathbf{f}(x, y) = [f_1(x, y), f_2(x, y), f_3(x, y)]$, which represents the image at a continuous scale and whose sampling yields its digital versions of any finite size.

Hence, once fixed the sampling model, that is the system of nodes

$$X_{\mu \times \nu} = \{(x_i^\mu, y_j^\nu)\}_{i=1:\mu, j=1:\nu}, \quad \mu, \nu \in \mathbb{N}, \quad (1)$$

we suppose that the digital image $I = [I_1, I_2, I_3]$ has behind the function $\mathbf{f} = [f_1, f_2, f_3]$ such that

$$I(i, j) = \mathbf{f}(x_i^{n_1}, y_j^{n_2}), \quad i = 1 : n_1, \quad j = 1 : n_2. \quad (2)$$

In both downscaling and upscaling the goal is getting an accurate reconstruction of I at a different (reduced and enhanced, resp.) size. Denoting by $N_1 \times N_2$ the new size that we aim to get and denoting by $R = [R_1, R_2, R_3]$ the target resized image of $N_1 \times N_2$ pixels, according to the previous settings, we have

$$R(i, j) = \mathbf{f}(x_i^{N_1}, y_j^{N_2}), \quad i = 1 : N_1, \quad j = 1 : N_2. \quad (3)$$

From this viewpoint, the scaling problem becomes a typical approximation problem: how to approximate the values of \mathbf{f} at the grid $X_{N_1 \times N_2}$ once known the values of \mathbf{f} at the finer (in downscaling) or coarser (in upscaling) grid $X_{n_1 \times n_2}$.

Within this setting, the choice of the nodes system (1) as well as the choice of the approximation tool are both decisive for the success of a scaling method. In the next subsections we are going to introduce these two basic ingredients and the evaluation metrics we use for our scaling method.

3.1 Sampling system

Since it is well-known that any finite interval $[a, b]$ can be mapped onto $[-1, 1]$, in the following we suppose that each spatial coordinate belongs to the reference interval $[-1, 1]$, so that the sampling system in (1) is included in the square $[-1, 1]^2$.

In literature the equidistant nodes model is usually adopted for sampling. According to such model, in (1) the coordinates $\{x_i^\mu\}_i$ and $\{y_j^\nu\}_j$ are those nodes that divide the segment $[-1, 1]$ into $(\mu + 1)$ and $(\nu + 1)$ equal parts, respectively. On the other hand, we recall that other coherent choices of the sampling system (1) have been recently investigated, for instance, in [13], [42] for Magnetic Particle Imaging.

Here we follow the sampling model recently introduced in [34]. The basic idea is to transfer the sampling question from the segment to the unit semicircle which is divided in equal arcs. More explicitly, we assume that (1) is the Chebyshev grid where the coordinates $\{x_i^\mu\}_i$ and $\{y_j^\nu\}_j$ are the zeros of the Chebyshev polynomial of first kind of degree μ and ν , respectively. This means that in (1) we are going to assume that

$$x_i^\mu = \cos(t_i^\mu) \quad \text{and} \quad y_j^\nu = \cos(t_j^\nu) \quad (4)$$

where, for all $n \in \mathbb{N}$, it is

$$t_k^n = \frac{(2k-1)\pi}{2n}, \quad k = 1 : n. \quad (5)$$

3.2 Filtered VP interpolation

Regarding the approximation tool underlying our method, we consider some filtered interpolation polynomials recently studied in [38]. Such kind of interpolation is based on a generalization of the trigonometric de la Vallée Poussin (VP) means (see [14, 55]) and, besides the number of nodes, it depends on two additional parameters which can be suitable modulated in order to strongly reduce the Gibbs phenomenon (see [38, 52]).

More precisely, for any $n_i, m_i \in \mathbb{N}$ such that $m_i < n_i$, $i = 1, 2$, let

$$\mathbf{n} = (n_1, n_2), \quad \text{and} \quad \mathbf{m} = (m_1, m_2),$$

and let n, m denote indifferently the first components (i.e. n_1, m_1 resp.) or the second components (i.e. n_2, m_2 resp.) of such vectors. Corresponding to these parameters, for any $r = 0 : (n-1)$, we define the following *orthogonal VP polynomials*

$$q_{m,r}^n(\xi) = \begin{cases} \cos(rt) & \text{if } 0 \leq r \leq (n-m), \\ \frac{n+m-r}{2m} \cos(rt) + \frac{n-m-r}{2m} \cos((2n-r)t) & \\ \text{if } n-m < r < n, \end{cases} \quad (6)$$

where here and in the following $\xi \in [-1, 1]$ and $t \in [0, \pi]$ are related by $\xi = \cos t$.

We recall the polynomial system in (6) consists of n univariate algebraic polynomials of degree at most $(n+m-1)$ that are orthogonal with respect to the scalar product

$$\langle F, G \rangle = \int_{-1}^1 F(\xi)G(\xi) \frac{d\xi}{\sqrt{1-\xi^2}}.$$

They generate the space (of dimension n)

$$S_m^n := \text{span}\{q_{m,r}^n : r = 0 : (n-1)\}$$

that is an intermediate polynomial space nested between the sets of all polynomials of degree at most $n-m$ and $n+m-1$.

The space S_m^n has also an interpolating basis consisting of the so-called *fundamental VP polynomials* that, in terms of the orthogonal basis (6), have the following expansion [52], [38]

$$\Phi_{m,k}^n(\xi) = \frac{2}{n} \left[\frac{1}{2} + \sum_{r=1}^{n-1} \cos(rt_k^n) q_{m,r}^n(\xi) \right], \quad k = 1 : n. \quad (7)$$

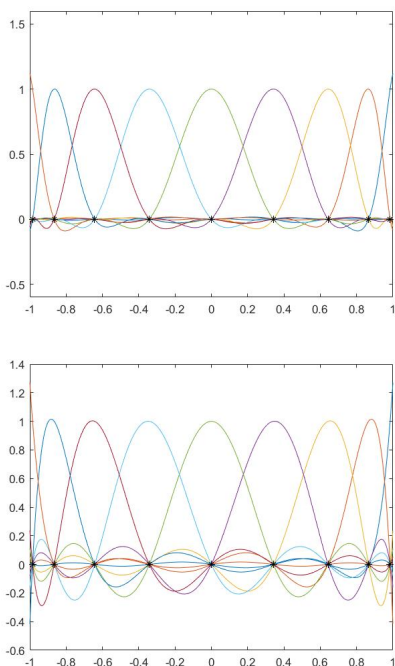


Fig. 1: Fundamental VP polynomials $\{\Phi_{m,k}^n\}_{k=1}^n$ for $n = 9$ and $m = 5$ (up), and fundamental Lagrange polynomials $\{\ell_{n,k}\}_{k=1}^n$ (down)

In Fig. 1 are plotted the fundamental VP polynomials for $n = 9$ and $m = 5$ (up) and for the same $n = 9$, the well-known fundamental Lagrange polynomials (down), defined as

$$l_{n,k}(\xi) = \frac{2}{n} \left[\frac{1}{2} + \sum_{r=1}^{n-1} \cos(rt_k^n) \cos(rt) \right], \quad k = 1 : n. \quad (8)$$

We see that, similarly to $\{l_{n,k}(\xi)\}_{k=1}^n$ also the fundamental VP polynomials satisfy the interpolation property

$$\Phi_{m,k}^n(\cos t_h^n) = l_{n,k}(\cos t_h^n) = \begin{cases} 1 & h = k \\ 0 & h \neq k \end{cases} \quad (9)$$

for all $h, k = 1 : n$.

In addition to the number n of nodes, we also have the free parameter m which can be arbitrarily chosen ($m = 1 : (n-1)$ being possible) without loosing the interpolation property (9), as stated in [52].

We recall in [7] both n, m are chosen depending on a resolution level $\ell \in \mathbb{N}$ and the fundamental VP polynomials constitute the scaling functions generating the multiresolution spaces $V_\ell = S_m^n$.

Another choice of m , often suggested in literature, is the following (see e.g. [37], [36])

$$m = \lfloor \theta n \rfloor, \quad \text{with } \theta \in]0, 1[, \quad (10)$$

where, $\forall a \in \mathbb{R}^+$, $\lfloor a \rfloor$ denotes the largest integer not greater than a .

Typically, for the convergence analysis, in (10), $n \rightarrow \infty$ and θ is arbitrarily fixed. Nevertheless in our case, we recall n is fixed since it is one of the dimensions of the RGB components $I_k \in \mathbb{R}^{n_1 \times n_2}$, $k = 1 : 3$, of the image I we aim to resize. Hence, we base our method on the following choice of the free parameter $\mathbf{m} = (m_1, m_2)$

$$m_i = \lfloor \theta n_i \rfloor, \quad i = 1, 2, \quad (11)$$

where we let θ to vary and we report in the experimental results the best values we get (see Section 6, item 4).

Figure 2 displays the plots of the fundamental VP polynomials corresponding to fixed n, k and m given by (10) with different values of θ . Indeed such parameter (and more generally m) is responsible of the localization of the fundamental VP polynomial $\Phi_{n,k}^m(\xi)$ around the node $\xi_k^n = \cos t_k^n$. In fact by Figure 2 we can see how those oscillations typical of the fundamental Lagrange polynomial $\ell_{n,k}$ (plotted too) are very dampened by suitable choices of θ .

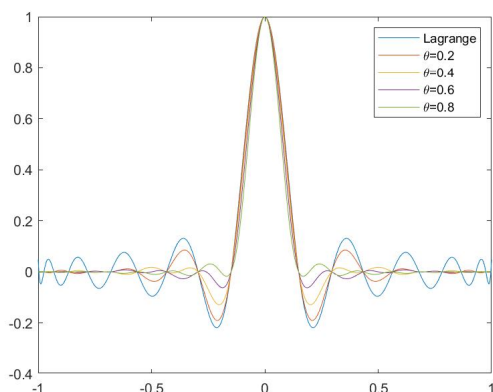


Fig. 2: Fundamental polynomials $\ell_{n,k}$ and $\Phi_{m,k}^n$ for $n = 21$, $k = 11$ and $m = \lfloor n\theta \rfloor$, with $\theta \in \{0.2, 0.4, 0.6, 0.8\}$.

By using the fundamental VP polynomials (7) we can approximate any function $g(x, y)$ on the square $[-1, 1]^2$ by means of its samples at the Chebyshev grid (1) as follows

$$V_{\mathbf{n}}^{\mathbf{m}}g(x, y) := \sum_{i=1}^{n_1} \sum_{j=1}^{n_2} g(x_i^{n_1}, y_j^{n_2}) \Phi_{n_1, i}^{m_1}(x) \Phi_{n_2, j}^{m_2}(y). \quad (12)$$

This is the definition of the *VP polynomial of g* and the approximation tool we use in our method.

By virtue of (9), such polynomial coincides with g at the grid $X_{n_1 \times n_2}$, i.e.

$$V_{\mathbf{n}}^{\mathbf{m}}g(x_i^{n_1}, y_j^{n_2}) = g(x_i^{n_1}, y_j^{n_2}), \quad i = 1 : n_1, \quad j = 1 : n_2, \quad (13)$$

Moreover, it has been proved that for any $(x, y) \in [-1, 1]^2$, if (11) holds with an arbitrarily fixed $\theta \in]0, 1[$ then for all continuous functions g , the following limit holds uniformly on $[-1, 1]^2$

$$\lim_{\mathbf{n} \rightarrow \infty} |V_{\mathbf{n}}^{\mathbf{m}}g(x, y) - g(x, y)| = 0$$

with the same convergence rate of the error of best polynomial approximation of g [38, Th.3.1].

3.3 Quality metrics

Similarly to most of the existing methods in literature, the performance of our method is quantitatively evaluated and compared with other scaling methods in terms of the Peak-Signal-to-Noise-Ratio (PSNR) and the Structural Similarity Index (SSIM). For our method such metrics will give a measure of the error between the target resized image $R = [R_1, R_2, R_3]$ and the output resized image that in the following we denote by $\tilde{R} = [\tilde{R}_1, \tilde{R}_2, \tilde{R}_3]$.

The definition of PSNR is based on the standard definition of the Mean Squared Error between two matrices

$$\text{MSE}(A, B) = \frac{1}{\nu\mu} \|A - B\|_F^2, \quad \forall A, B \in \mathbb{R}^{\nu \times \mu} \quad (14)$$

being $\|\cdot\|_F$ the Frobenius norm defined as

$$\|A\|_F := \left(\sum_{h=1}^{\nu} \sum_{k=1}^{\mu} a_{h,k}^2 \right)^{\frac{1}{2}}, \quad \forall A = (a_{h,k}) \in \mathbb{R}^{\nu \times \mu}.$$

The extension of such definition to the case of color digital images of $\nu \times \mu$ pixels can be performed in different ways giving rise to different measures of the related

PSNR (see e.g. [47, 70]). More precisely, for the color images R and \tilde{R} , defining their MSE as follows

$$\text{MSE}(\tilde{R}, R) = \frac{1}{3} \sum_{k=1}^3 \text{MSE}(\tilde{R}_k, R_k) \quad (15)$$

the first, usually adopted definition of PSNR (used for instance in [34]) is the following

$$\text{PSNR}(\tilde{R}, R) = 20 \log_{10} \left(\frac{\max_f}{\sqrt{\text{MSE}(\tilde{R}, R)}} \right). \quad (16)$$

Another common way to measure the PSNR (also used in [60]) is given by converting to the color space YCrCb both the color RGB images $R = [R_1, R_2, R_3]$ and $\tilde{R} = [\tilde{R}_1, \tilde{R}_2, \tilde{R}_3]$, and separating the intensity Y (luma) channels that we denote by R_Y and \tilde{R}_Y , respectively. We recall they are defined by the following weighted average of the respective RGB components

$$R_Y = \sum_{k=1}^3 \alpha_k R_k + \alpha_4, \quad \tilde{R}_Y = \sum_{k=1}^3 \alpha_k \tilde{R}_k + \alpha_4, \quad (17)$$

with α_i , $i = 1 : 4$ coefficients of the ITU -R BT.601 standard (see e.g. [4]). Hence, taking the MSE of the matrices R_Y and \tilde{R}_Y , the second, commonly used, definition of PSNR is referred to only such luma channel as follows

$$\text{PSNR}(\tilde{R}, R) = 20 \log_{10} \left(\frac{\max_f}{\sqrt{\text{MSE}(\tilde{R}_Y, R_Y)}} \right), \quad (18)$$

We point out that in our experiments the PSNR has been computed using both the previous definitions. However, for brevity, in this paper we report only the values achieved by the definition (18), giving no new insight the results obtained by using the other definition (16).

Finally, also the SSIM metric is defined via the luma channel as follows [61]

$$\text{SSIM}(\tilde{R}, R) = \frac{[2\tilde{\mu}\mu + c_1][2\text{cov} + c_2]}{[\tilde{\mu}^2 + \mu^2 + c_1][\tilde{\sigma}^2 + \sigma^2 + c_2]}, \quad (19)$$

where $\tilde{\mu}, \mu$ and $\tilde{\sigma}, \sigma$ denote the average and variance of the matrices \tilde{R}_Y, R_Y , respectively, cov indicates their covariance, and the constants are usually fixed as $c_1 = (0.01 \times L)$, $c_2 = (0.03 \times L)$ with the dynamic range of the pixel values $L = 255$ in the case of 8-bit images.

4 VPI scaling method

According to the notation introduced in the previous section, both I and R are digital versions (with $n_1 \times n_2$ and $N_1 \times N_2$ pixels, respectively) of the same continuous image represented by the vector function $\mathbf{f} = (f_1, f_2, f_3)$ (cf. (2), (3)). Nevertheless, to be more general, in view of the finite representation of the data and the accuracy used to store the images, we suppose the effective input image of our method is a more or less corrupted version of I . We denote it by $\tilde{I} = [\tilde{I}_1, \tilde{I}_2, \tilde{I}_3]$ and assume that there exists a corrupted function $\tilde{\mathbf{f}} = (\tilde{f}_1, \tilde{f}_2, \tilde{f}_3)$ such that

$$\tilde{I}(i, j) = \tilde{\mathbf{f}}(x_i^{n_1}, y_j^{n_2}), \quad i = 1 : n_1, \quad j = 1 : n_2. \quad (20)$$

Starting from these initial data, VPI method computes the output image \tilde{R} having the desired size $N_1 \times N_2$ and defined as follows

$$\tilde{R}(i, j) = V_{\mathbf{n}}^{\mathbf{m}} \tilde{\mathbf{f}}(x_i^{N_1}, y_j^{N_2}), \quad i = 1 : N_1, \quad j = 1 : N_2. \quad (21)$$

In terms of the RGB components $\tilde{R} = [\tilde{R}_1, \tilde{R}_2, \tilde{R}_3]$, by (12), this means that for any $i = 1 : N_1$, $j = 1 : N_2$ and $k = 1 : 3$ we have

$$\begin{aligned} \tilde{R}_k(i, j) &= V_{\mathbf{n}}^{\mathbf{m}} \tilde{f}_k(x_i^{N_1}, y_j^{N_2}) = \\ &= \sum_{u=1}^{n_1} \sum_{v=1}^{n_2} \tilde{I}_k(u, v) \Phi_{n_1, u}^{m_1}(x_i^{N_1}) \Phi_{n_2, v}^{m_2}(y_j^{N_2}), \end{aligned} \quad (22)$$

that is

$$\tilde{R}_k = V_1^T \tilde{I}_k V_2, \quad k = 1 : 3, \quad (23)$$

where the matrices $V_1 \in \mathbb{R}^{n_1 \times N_1}$ and $V_2 \in \mathbb{R}^{n_2 \times N_2}$ have the following entries

$$V_1(i, j) = \Phi_{n_1, i}^{m_1}(x_j^{N_1}), \quad i = 1 : n_1, \quad j = 1 : N_1 \quad (24)$$

$$V_2(i, j) = \Phi_{n_2, i}^{m_2}(y_j^{N_2}), \quad i = 1 : n_2, \quad j = 1 : N_2 \quad (25)$$

To compute V_1, V_2 an efficient algorithm based on Fast Fourier transforms can be implemented. By pre-computing matrices V_i , the representation (23) allows to a strong reduction in the computational effort in the case we have to resize a lot of images for the same fixed sizes. Moreover, parallel computing algorithms can be also employed.

Now, we note that in (24-25) the integers n_ℓ and N_ℓ for $\ell = 1, 2$ are determined by the initial and final size of the scaling problem we have while, so far, the parameter m_ℓ is free. Theoretically, it can be arbitrarily chosen from the set of integers between 1 and $(n_\ell - 1)$ and it could be also provided by the user as an input parameter. Nevertheless, we have structured our method in adaptive way looking for adapting the choice of m_ℓ to the specific image that we have to resize from

time to time. To this aim, as announced in the previous section, we have fixed

$$m_\ell = \lfloor \theta n_\ell \rfloor, \quad \ell = 1, 2.$$

Hence, taking different choices of $\theta \in]0, 1[$ we get several matrices V_1, V_2 that determine, by means of (23), several resized images. Among these images, the one that, once compared with the target image R , gives the smallest MSE is chosen as output image of our method.

According to such an optimization procedure the only input arguments of VPI methods are the input image \tilde{I} and the final size, namely the integers $N_1, N_2 \in \mathbb{N}$ that can be either explicitly given by the user or determined by the input scale factor. This is defined throughout the paper as follows

$$s = \begin{cases} \frac{n_1}{N_1} = \frac{n_2}{N_2} & \text{if } n_1 > N_1 \text{ (downscaling factor)} \\ \frac{N_1}{n_1} = \frac{N_2}{n_2} & \text{if } n_1 < N_1 \text{ (upscaling factor)} \end{cases}$$

Finally, in all the cases that the downscaling factor is odd, we state the following

Proposition 1 *Let I and R be the initial and resized true images given by (2) and (3) respectively, and let \tilde{I} and \tilde{R} by input and output images of d -VPI method, respectively given by (20) and (21), with arbitrarily fixed integer parameters $m_1 < n_1$ and $m_2 < n_2$. If there exists $\ell \in \mathbb{N}$ that relates the initial size $n_1 \times n_2$ with the final size $N_1 \times N_2$ as follows*

$$\frac{n_1}{N_1} = \frac{n_2}{N_2} = (2\ell - 1), \quad (26)$$

then we have

$$\text{MSE}(R, \tilde{R}) \leq s^2 \text{MSE}(I, \tilde{I}), \quad s = (2\ell - 1). \quad (27)$$

The same estimate holds also for the luma channel and, if in addition $I = \tilde{I}$ holds too, then we get

$$\text{PSNR}(R, \tilde{R}) = \infty, \quad \text{and} \quad \text{SSIM}(R, \tilde{R}) = 1. \quad (28)$$

Proof. Recalling the definition (15), to prove (27) it is sufficient to state the same inequality holds for the respective RGB components. Hence, according to our notation, let us state that for all $k = 1 : 3$ we have

$$\text{MSE}(R_k, \tilde{R}_k) < s^2 \text{MSE}(I_k, \tilde{I}_k). \quad (29)$$

To this aim, by using the short notation n and N to denote n_i and N_i , respectively, for any $i = 1, 2$, we note that whenever we have $n = sN$ with $s = (2\ell - 1)$ and $\ell \in \mathbb{N}$, all the zeros of the first kind Chebyshev polynomial of degree N (i.e. $\cos(t_h^N)$ with $h = 1 : N$) are also zeros of the first kind Chebyshev polynomial of degree n . More precisely, we have

$$\cos(t_h^N) = \cos(t_{i(h)}^n) \quad \text{with} \quad i(h) = \frac{s(2h - 1) + 1}{2}, \quad (30)$$

where we point out that for all $h = 1 : N$ the index $i(h) = \frac{s(2h-1)+1}{2}$ is an integer between 1 and n thanks to the hypothesis s is odd.

By virtue of (30), for all $h_1 = 1 : N_1$ and $h_2 = 1 : N_2$, recalling (3)–(5) we get

$$\begin{aligned} R_k(h_1, h_2) &= f_k \left(x_{h_1}^{N_1}, y_{h_2}^{N_2} \right) \\ &= f_k \left(x_{i(h_1)}^{n_1}, y_{i(h_2)}^{n_2} \right) \\ &= I_k(i(h_1), i(h_2)) \end{aligned} \quad (31)$$

Similarly, from (21), (30), (13) and (20), we deduce

$$\begin{aligned} \tilde{R}_k(h_1, h_2) &= V_{\mathbf{n}}^{\mathbf{m}} \tilde{f}_k \left(x_{h_1}^{N_1}, y_{h_2}^{N_2} \right) \\ &= V_{\mathbf{n}}^{\mathbf{m}} \tilde{f}_k \left(x_{i(h_1)}^{n_1}, y_{i(h_2)}^{n_2} \right) = \tilde{f}_k \left(x_{i(h_1)}^{n_1}, y_{i(h_2)}^{n_2} \right) \\ &= \tilde{I}_k(i(h_1), i(h_2)) \end{aligned} \quad (32)$$

Therefore, by (31) and (32), for any $k = 1 : 3$ we deduce (29) as follows

$$\begin{aligned} \text{MSE}(R_k, \tilde{R}_k) &= \\ &= \frac{1}{N_1 N_2} \sum_{h_1=1}^{N_1} \sum_{h_2=1}^{N_2} \left[R_k(h_1, h_2) - \tilde{R}_k(h_1, h_2) \right]^2 \\ &= \frac{1}{N_1 N_2} \sum_{h_1=1}^{N_1} \sum_{h_2=1}^{N_2} \left[I_k(i(h_1), i(h_2)) - \tilde{I}_k(i(h_1), i(h_2)) \right]^2 \\ &\leq \frac{1}{N_1 N_2} \sum_{i=1}^{n_1} \sum_{j=1}^{n_2} \left[I_k(i, j) - \tilde{I}_k(i, j) \right]^2 \\ &= \frac{s^2}{n_1 n_2} \sum_{i=1}^{n_1} \sum_{j=1}^{n_2} \left[I_k(i, j) - \tilde{I}_k(i, j) \right]^2 \\ &= s^2 \text{MSE}(I_k, \tilde{I}_k). \end{aligned}$$

As regards the luma channel, we note that by (31)–(32) and (17) we easily deduce that

$$\begin{aligned} R_Y(h_1, h_2) &= I_Y(i(h_1), i(h_2)) \\ \tilde{R}_Y(h_1, h_2) &= \tilde{I}_Y(i(h_1), i(h_2)) \end{aligned} \quad (33)$$

and such identities, similarly to the case of the RGB components, easily imply

$$\text{MSE}(R_Y, \tilde{R}_Y) \leq s^2 \text{MSE}(I_Y, \tilde{I}_Y) \quad (34)$$

Finally, in the case that $I = \tilde{I}$, from (31) and (32) we deduce that

$$R_k(h_1, h_2) = \tilde{R}_k(h_1, h_2), \quad k = 1 : 3$$

holds for any $h_1 = 1 : N_1$ and $h_2 = 1 : N_2$. Consequently we get the best result (28). \diamond

Remark 1 By the previous proof, the reader can realize that the hypothesis $I = \tilde{I}$ can be relaxed requiring that these images coincide only on some suitable pixels. In fact, in order to get (28) it is sufficient that

$$\begin{aligned} I_k(i(h_1), i(h_2)) &= \tilde{I}_k(i(h_1), i(h_2)), \\ k = 1 : 3, \quad h_1 = 1 : N_1, \quad h_2 = 1 : N_2 \end{aligned} \quad (35)$$

holds, where we defined

$$i(h) = \frac{s(2h-1)+1}{2}. \quad (36)$$

5 Experimental Results

In this section, we describe the experimental validation of VPI. Specifically, Section 5.1 introduces the considered datasets; Sections 5.2 and 5.3 are devoted to qualitative and quantitative performance evaluation, respectively, both in downscaling and upscaling; Section 5.4 concerns further experimentation for d-VPI.

In the following, we premise some common aspects and implementation details.

1. We have tested VPI on some publicly available image datasets by performing comparisons with the methods described in Section 2; namely, we compare d-VPI with BIC, d-LCI, L₀, DPID, and u-VPI with BIC, u-LCI, SCN. To be more general, besides the datasets used by the comparison methods [18, 23, 34, 60, 62], we also consider some datasets extensively employed for image analysis tasks. In this way, d-VPI and u-VPI are evaluated on many image datasets offering different characteristics.
2. BIC is implemented by the Matlab built-in function `imresize` with `bicubic` option. For the other methods, we used the publicly available Matlab codes provided by the authors with the default parameters settings.
3. When the input images are not available in the considered datasets, we have magnified (reduced) the target $N_1 \times N_2$ image by `imresize`, originating the input $n_1 \times n_2$ image used for all downscaling (upscaling) methods. In the upscaling analysis, whenever N_1 or N_2 is not divisible for the scale factor s , the input image is generated by `imresize` setting $n_1 = \left\lfloor \frac{N_1}{s} \right\rfloor$ and $n_2 = \left\lfloor \frac{N_2}{s} \right\rfloor$.
4. In VPI Matlab code, by default, the free parameter $\mathbf{m} = (m_1, m_2)$ is chosen according to (11) with θ varying from 0.05 to 0.95 with step 0.05. In this way, we get 19 resized images, and we take as output image that one with the minimum MSE.

5. Similar to LCI and `imresize`, also VPI code returns the LR (HR) image by specifying the scale factor or the desired size.
6. Although DPID and L_0 (SCN) can be also applied in upscaling (downscaling) mode, we do not force the comparison with them in an unplanned way to avoid an incorrect experimental evaluation.
7. All methods have run on the same computer with the configuration Intel Core i7 3770K CPU @350GHz in Matlab 2018a.

5.1 Datasets

The d-VPI performance evaluation is carried out on some publicly available datasets, comprising 726 color images in total. In particular, we consider BSDS500 dataset [27], available at [71] which includes 500 color images having the same size (481×321 or 321×481). This set, also used in [23, 34], is sufficiently general and provides a large variety of images often employed also in other different image analysis tasks, such as in image segmentation [32, 44–46] and in color quantization [6, 8, 48, 49].

To favor the comparison with the other methods, we also consider the following datasets.

- The 13 natural-color images of the user study in [41], available at [72] and here denoted by 13US. They are originally taken from the MSRA Salient Object Database [24], used in a previous study [19] and also employed in [62]. These images, displayed in Figure 3, have sizes ranging from 241×400 to 400×310 pixels.
- The extensive two sets selected in [62] from the Yahoo 100Mimage dataset [56] and the NASA Image Gallery [73], available at [74]. We denote by NASA and YAHOO the corresponding sets of color images extracted from them. These sets comprise 17 and 96 color images, with sizes ranging from 500×334 to 6394×3456 , respectively. The NASA dataset images are shown in Figure 4.
- The Urban100 dataset [17] including 100 color images related to an urban context, with one dimension at most equal to 1024 and the other ranging from 564 to 1024 pixels. It has also been employed in [23].

Regarding the u-VPI performance evaluation, in addition to the previous datasets, we have also used the following well-known datasets, commonly used by the Super Resolution community [16, 20].

- The 5 images, known in the literature, as Set5 and originally taken from [3], with size ranging from

256×256 to 512×512 . They are displayed in Figure 5.

- The 12 color images belonging to the Set14 [67], with size ranging from 276×276 to 512×768 . These images are shown in Figure 6.
- The image dataset DIV2k (DIVERse 2k) consisting of high-quality resolution images used for the NTIRE 2017 SR challenge (CVPR 2017 and CVPR 2018) [57] available at [75]. It comprises the train set (DIV2k-T) and the valid set (DIV2k-V), with 800 and 100 color images, respectively. Such images have one dimension equal to 2040, while the other one ranges from 768 to 2040. DIV2k has permitted to test the performance of all the benchmark methods on input images characterized by different types of degradations. Such input images are included in DIV2k and collected as follows:
 - DIV2k-T-B (DIV2k-V-B), generated by BIC (-B);
 - DIV2k-T-u (DIV2k-V-u), classified as unknown (-u);
 - DIV2k-T-d (DIV2k-V-d), classified as difficult (-d);
 - DIV2k-T-m (DIV2k-V-m), classified as mild (-m).

5.2 Qualitative evaluation

For the qualitative evaluation, we test VPI and the benchmark methods, for scale factors varying from 2 to very large values. Some visual results of the numerous tests are given in Figures 7-8 for d-VPI and in Figures 9-10 for u-VPI for different input images with scale factors 2, 3, 4. Some Regions of Interest (ROI) are shown in order to highlight the results at a visual level.

By visually inspecting the performance results (e.g., see Figure 6 and Figure 8), we deduce that: a) the visual structure of the objects is captured; b) local contrast and luminance of the input image are preserved; c) small details and most of the salient edges are maintained; d) the presence of ringing and over smoothing artifacts is very limited; e) the resized image is sufficiently not blurred.

5.3 Downscaling quantitative evaluation

To quantitatively evaluate d-VPI, we compute the visual quality measures PSNR, SSIM, and the CPU time T for different scale factors. The average downscaling performance results for each dataset are shown in Table 1 and graphically represented in Figure 11. From these results, it is possible to verify that:



Fig. 3: 13US dataset images: [U1 -U13] from left to right and from top to bottom with size ranging from 241×400 to 400×310 pixels.

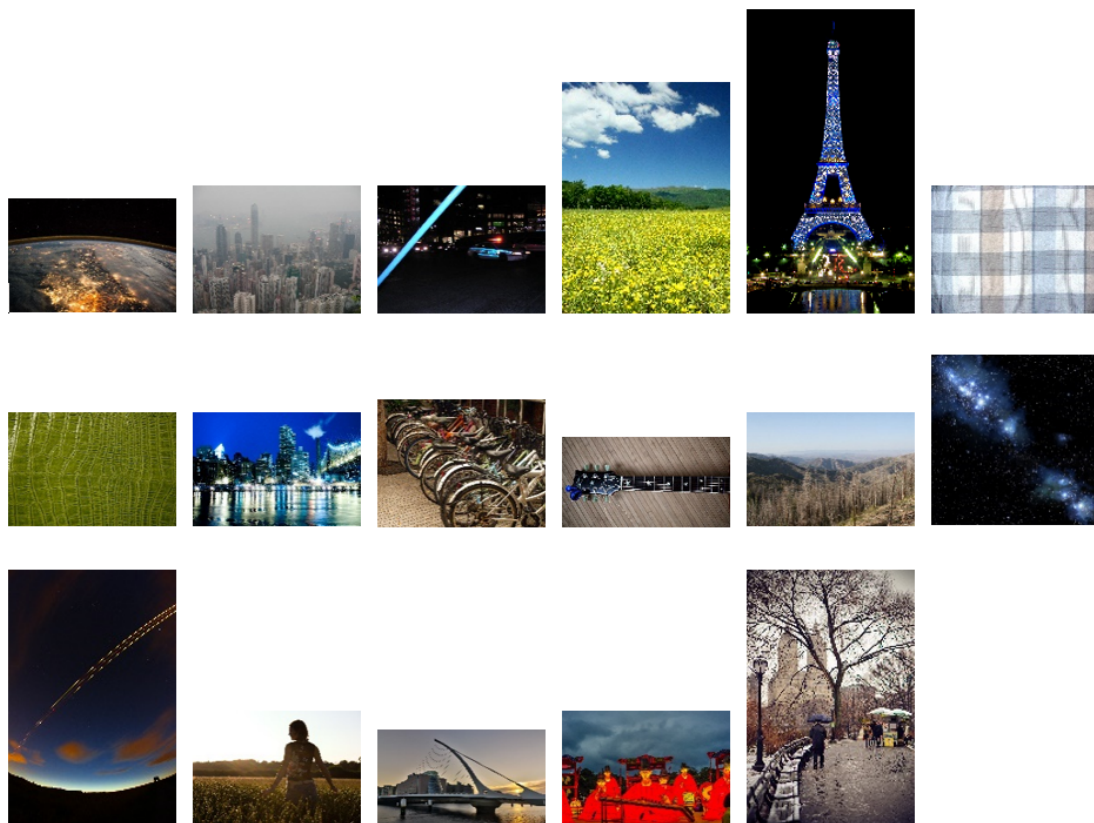


Fig. 4: NASA dataset images: [N1, N2, N3, N5, N6, N7, N8, N9, N10, N11, N12, N13, N14, N15, N16, N17, N19] from left to right and from top to bottom with different size ranging from 500×334 to 6394×3456 (see Table 1)

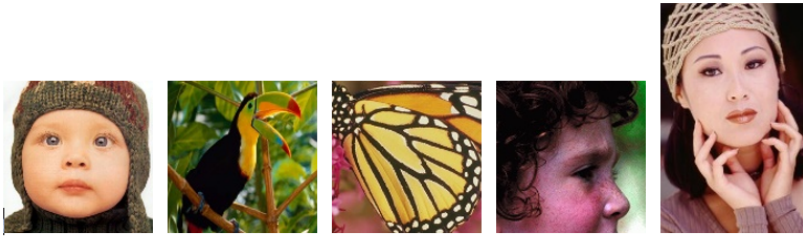


Fig. 5: Set5 dataset images: [S5.1, S5.2, S5.3, S5.4, S5.5] from left to right and from top to bottom with different size ranging from 256×256 to 512×512 .

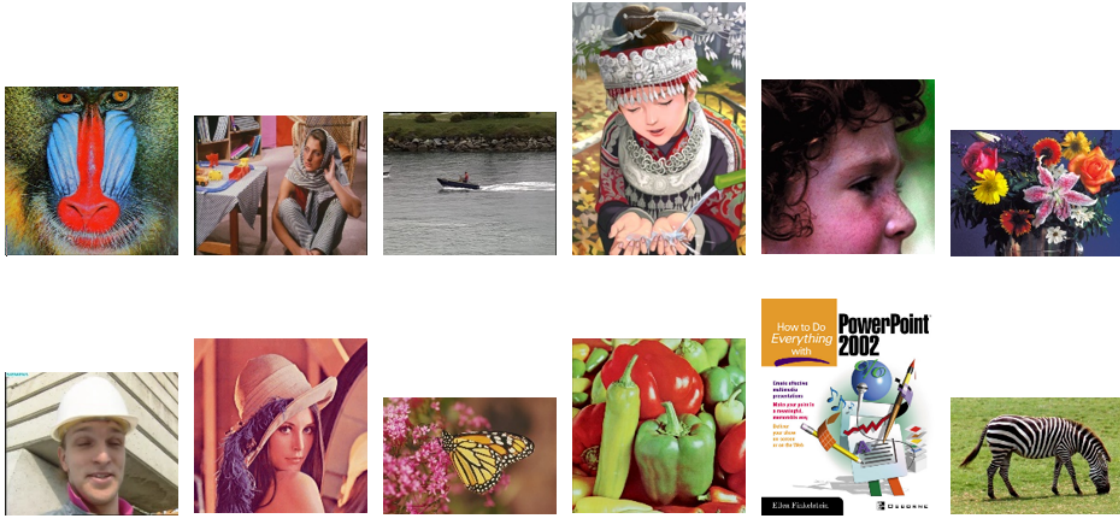


Fig. 6: Set14 dataset images: [S14.1, S14.2, S14.4, S14.5, S14.6, S14.7, S14.8, S14.9, S14.11, S14.12, S14.13, S14.14] from left to right and from top to bottom with different size ranging from 276×276 to 510×768

- d.1 The best PSNR and SSIM values are achieved by d-VPI, followed in order by d-LCI (ex-aequo in some cases), DPID, BIC, and L_0 in all datasets for all scale factors.
- d.2 For all scale factors, there is a consistent gap between the PSNR values by d-VPI and those provided by L_0 , DPID, and BIC. As pointed out in [34], also d-LCI provides good results, but generally, d-VPI outperforms d-LCI, even if with a smaller gap. For instance, for the dataset BSDS500 and $s = 2$, the gap between d-VPI and BIC is $16db$, reaching the maximum value of $26db$ between L_0 and d-VPI while the gap with d-LCI is far less, providing such method already better than the others (BIC, DPID, and L_0).
- d.3 When $s = 3$, the theoretical result proved in Proposition 1 is confirmed. We note that this case is missing in Figure 11 since (28) holds for both d-LCI and d-VPI. Nevertheless, we point out that such

an optimal performance has been proved under the assumption $I = \tilde{I}$ (or more generally (35)) and hence it is not always true. Indeed we have verified (28) continues to hold starting from HR input images generated by the Nearest-Neighbor and Bilinear methods [15] (using Matlab `imresize` with `nearest` and `bicubic` option respectively), but it does not hold, for instance, if we use SCN to generate the input HR image. Moreover, we remark that since d-LCI requires less CPU time than d-VPI it is clearly more convenient to use d-LCI instead of d-VPI whenever they provide the same values as in this case.

- d.4 Going from $s = 2$ to $s = 4$, we see that the bars in Figure 11 become higher for all methods except for DPID that, indeed, get worse. For all the methods, we measure in percentage such discrepancy by the

following formula

$$\Delta = \frac{100}{q} \sum_{i=1}^q \frac{P_i(4) - P_i(2)}{P_i(4)}$$

where $q = 5$ and $P_i(s)$ denotes the average PSNR value of the i -th dataset at the scale s . We find for d-VPI a value Δ nearly to 8.9%, while for d-LCI it is approximately 3.9%, for BIC it is only 0.9%, and for DPID, we have a negative Δ about -1%. L_0 is the method with the largest Δ (nearly to 18.35%) but NASA and YAHOO are excluded from the computation of Δ since L_0 does not give any output for such datasets. Moreover, for $s = 2$ the PSNR value of L_0 is so smaller that the bigger value achieved for $s = 4$ is in any case much smaller compared with d-VPI and also with the other methods.

- d.5 The method requiring the least computation time is BIC, but with lower values of PSNR and SSIM. In the second position, we find d-LCI with computation times close to those required by BIC. In the third position, d-VPI requires more time than d-LCI, especially in the case of large image size. This is due mainly to the optimization procedure we operate on the free parameter \mathbf{m} , as described at the beginning of this section, point 4. In the ranking, DPID and L_0 follow with much higher computation time than d-VPI, especially on datasets characterized by larger image sizes (such as NASA, YAHOO, and Urban100).

5.4 Upscaling quantitative evaluation

In Tables 2-3-4 are synthesized the average results of PSNR, SSIM values and the computation time for the scale factors 2,3,4. We remark that the comparison with SCN is limited to DIV2k since, for the other datasets, the SCN demo version does not always produce the exact size of the HR image, making it impossible to compute the quality measure values. Specifically, Table 3 and 4 concern the DIV2k dataset and also include the values by SCN, while Table 2 regards all the remaining datasets and, due to the aforesaid experimental limitations, it does not include SCN values. We remark that Table 4 concerns only the case $s = 4$ since for $s = 2, 3$ the input LR images are not present in DIV2k-T-d/m and DIV2k-V-d/m datasets. Moreover, the bar graphs describing the trend of the previous PSNR and SSIM values are shown in Figures 12 and 13.

From the displayed results, it is possible to verify that on average:

- u.1 In Table 2 u-VPI has a slightly higher performance than BIC and u-LCI in terms of visual quality values;
- u.2 Inspecting Table 3, we observe that the previous trend for BIC, u-LCI, and u-VPI is confirmed. The best visual quality values are those provided by SCN when the input images are generated by Bicubic, namely for DIV2k-T-B and DIV2k-V-B datasets. Nevertheless, in the case of input images classified unknown, namely for DIV2k-T-u and DIV2k-V-u datasets, slightly higher performance values are given by u-VPI, except one case (when $s=4$ for DIV2k-T-u).
- u.3 In Table 4 we note a different behavior. In this case, SCN always provides the lowest PSNR and SSIM values. For input images classified both difficult and mild, u-VPI continues to provide the best values for the Train images, namely DIV2k-T-d and DIV2k-T-m, but it is outperformed by BIC for the Valid images, namely DIV2k-V-d and DIV2k-V-m. Finally, no change regards the comparison u-VPI / u-LCI, where u-VPI always gives slightly higher values.
- u.4 The method requiring the least CPU time is BIC, followed by u-LCI with computation time quite close to it. Analogously to the downscaling mode, u-VPI requires a higher computation time but it is much less than SCN, which results to have the longest CPU time.

5.5 Futher downscaling quantitative evaluation

In this subsection, we analyze in more detail some features offered by d-VPI in comparison with the other methods.

For the scale factors 2, 3, 4, besides the average results shown in Table 1, we report in Table 5 the pointwise values of PNSR, SSIM obtained by each downscaling method for randomly selected images from 13US and NASA datasets (5 images for each dataset). Moreover, for any selected image, in the last column of Table 5, we report the value

$$\delta = 100 \frac{p(4) - p(2)}{p(4)}$$

where $p(s)$ denotes the PSNR value achieved for that image at the scale s .

The analysis of Table 5 shows that the pointwise results confirm the trend expresses by Table 1 and the comments given for the average results continue to hold. In particular, the values of δ confirm that, as already remarked at the previous point d.4, the improvement



Fig. 7: Examples of downscaling performance results at the scale factor 2 (left), at the scale factor 3 (middle), at the scale factor 4 (right).

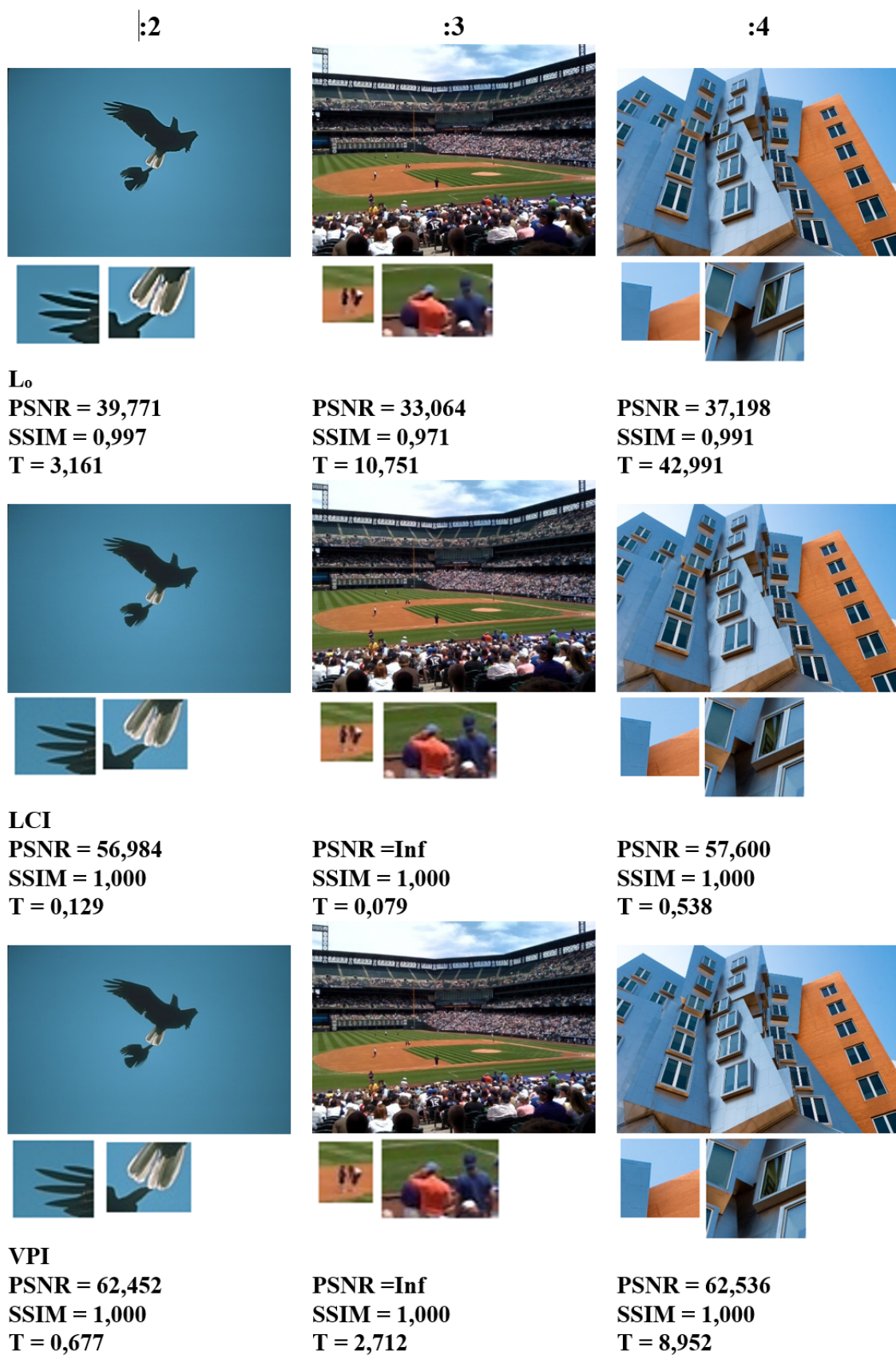


Fig. 8: Examples of downscaling performance results at the scale factor 2 (left), at the scale factor 3 (middle), at the scale factor 4 (right).



Fig. 9: Examples of upscaling performance results at the scale factor 2 (left), at the scale factor 3 (middle), at the scale factor 4 (right).

Table 1: Average performance results on the selected dataset in downscaling (oom is the short way to indicate "out of memory").

	:2			:3			:4		
	PSNR	SSIM	T	PSNR	SSIM	T	PSNR	SSIM	T
BSDS500									
BIC	40,152	0,993	0,006	40,526	0,993	0,009	40,456	0,993	0,017
DPID	43,011	0,996	7,696	43,090	0,996	12,246	42,481	0,996	18,615
L ₀	30,742	0,961	3,647	34,304	0,971	8,020	35,585	0,971	14,295
d-LCI	54,852	1,000	0,057	Inf	1,000	0,091	56,890	1,000	0,137
d-VPI	56,025	1,000	0,806	Inf	1,000	1,356	60,928	1,000	2,117
13US									
BIC	36,419	0,990	0,005	36,755	0,991	0,009	36,683	0,991	0,013
DPID	39,405	0,996	5,593	39,676	0,996	8,905	38,988	0,995	13,819
L ₀	27,008	0,949	2,572	31,637	0,972	5,706	34,467	0,979	9,939
d-LCI	54,172	1,000	0,042	Inf	1,000	0,073	56,541	1,000	0,108
d-VPI	55,039	1,000	0,466	Inf	1,000	0,748	59,529	1,000	1,132
NASA									
BIC	47,688	0,995	0,229	48,849	0,996	0,325	48,706	0,996	0,639
DPID	49,218	0,998	448,023	49,212	0,998	731,498	48,706	0,997	1.098,113
L ₀	36,461	0,972	208,574	39,043	0,979	617,386	oom	oom	oom
d-LCI	55,497	0,999	6,614	Inf	1,000	13,317	58,497	1,000	22,859
d-VPI	57,632	1,000	116,137	Inf	1,000	257,757	64,042	1,000	344,892
YAHOO									
BIC	46,261	0,996	0,155	47,371	0,997	0,219	47,189	0,996	0,422
DPID	48,187	0,998	291,685	48,398	0,998	479,638	47,901	0,998	714,908
L ₀	35,686	0,974	133,190	oom	oom	oom	oom	oom	oom
d-LCI	55,227	0,999	4,698	Inf	1,000	8,279	58,306	1,000	13,898
d-VPI	57,315	1,000	89,711	Inf	1,000	169,616	63,800	1,000	267,317
URBAN100									
BIC	37,071	0,989	0,027	37,414	0,990	0,041	37,344	0,989	0,068
DPID	40,648	0,996	37,592	40,858	0,996	60,834	40,192	0,995	93,996
L ₀	28,215	0,951	13,267	32,608	0,969	28,845	35,185	0,973	50,312
d-LCI	53,800	0,999	0,234	Inf	1,000	0,416	56,560	1,000	0,618
d-VPI	54,703	1,000	3,847	Inf	1,000	6,749	59,730	1,000	10,995

Table 2: Average performance results on the selected dataset in upscaling

	x2			x3			x4		
	PSNR	SSIM	T	PSNR	SSIM	T	PSNR	SSIM	T
BSDS500									
BIC	27,665	0,886	0,003	26,148	0,837	0,002	23,678	0,701	0,003
u-LCI	27,707	0,888	0,014	26,196	0,839	0,010	23,793	0,769	0,008
u-VPI	27,748	0,890	0,232	26,237	0,841	0,200	23,865	0,770	0,181
13US									
BIC	25,429	0,861	0,002	22,125	0,734	0,002	21,906	0,710	0,002
u-LCI	25,800	0,868	0,012	22,127	0,738	0,010	22,010	0,713	0,009
u-VPI	25,859	0,872	0,157	22,194	0,739	0,142	22,045	0,716	0,122
NASA									
BIC	37,638	0,958	0,091	32,298	0,924	0,074	32,232	0,907	0,071
u-LCI	38,485	0,960	1,357	34,910	0,924	0,839	32,793	0,908	0,634
u-VPI	38,540	0,961	19,454	34,976	0,927	13,931	32,830	0,910	11,086
YAHOO									
BIC	34,979	0,953	0,056	31,354	0,913	0,055	30,368	0,891	0,051
u-LCI	35,507	0,955	0,812	31,556	0,914	0,567	30,607	0,891	0,459
u-VPI	35,573	0,956	17,047	31,602	0,916	11,906	30,654	0,894	9,518
URBAN100									
BIC	26,860	0,882	0,009	22,737	0,755	0,008	23,135	0,741	0,008
u-LCI	27,321	0,886	0,051	22,755	0,754	0,051	23,350	0,793	0,059
u-VPI	27,387	0,891	1,016	22,802	0,759	0,800	23,388	0,748	0,135
Set5									
BIC	33,646	0,965	0,003	28,596	0,916	0,003	28,425	0,908	0,002
u-LCI	34,499	0,969	0,014	28,881	0,918	0,008	28,915	0,912	0,006
u-VPI	34,540	0,969	0,482	28,924	0,918	0,135	28,946	0,913	0,122
Set14									
BIC	30,375	0,917	0,003	27,597	0,839	0,003	26,022	0,807	0,005
u-LCI	31,020	0,921	0,020	28,026	0,841	0,014	26,333	0,809	0,013
u-VPI	31,080	0,923	0,300	28,064	0,843	0,253	26,371	0,812	0,234



Fig. 10: Examples of upscaling performance results at the scale factor 2 (left), at the scale factor 3 (middle), at the scale factor 4 (right).

from the scale $s = 2$ to $s = 4$ is faster for d-VPI followed by d-LCI and BIC, while DPID values get worse with negative δ . The method L_0 runs only for the small images from 13US, and in those cases, it has the biggest δ but the smallest PSNR values.

We have also tested the performance of d-VPI for scale factors greater than 4 on all datasets at hand. In this case, the comparison is restricted to BIC and u-LCI since the available code of DPID, and L_0 have un-

sustainable computation times and/or out-of-memory problems. In particular, Table 6 shows the performance results for the scale factor 10, 15, 30 on the images of 13US dataset whose size is suitable for high scale factors. Note that when $s = 30$, we have to provide an input image whose size is 30 times bigger than that of the image in the dataset, hence by 13US dataset, we arrive to consider input images of 12000×9300 pixels.

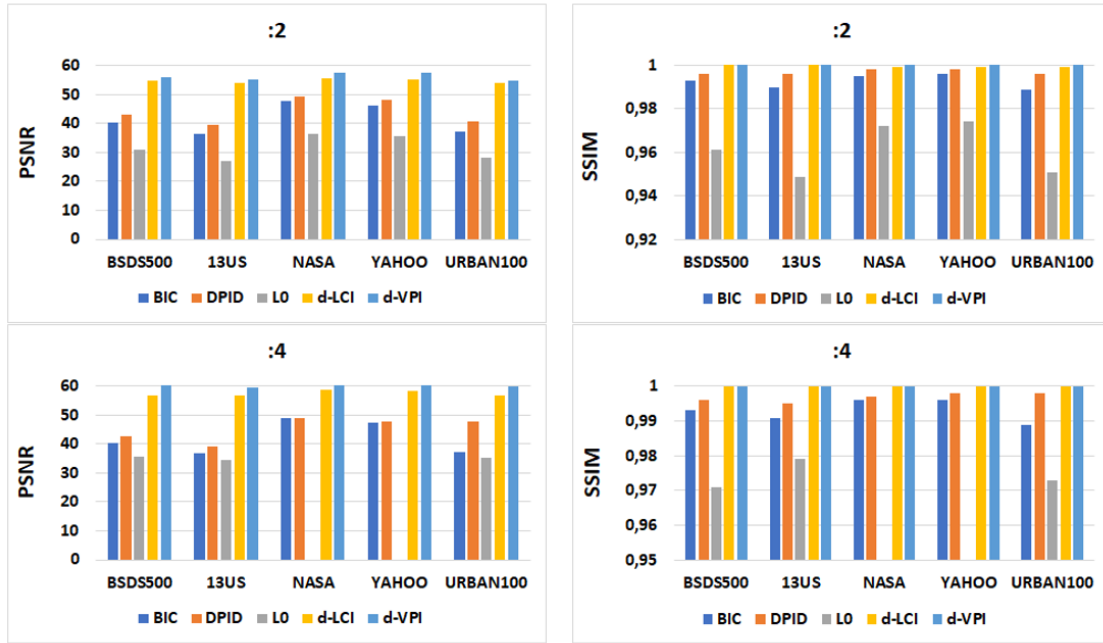


Fig. 11: PSNR and SSIM values for the scale factor 2 (top) and for the scale factor 4 (bottom), respectively, extracted from Table 1. PSNR and SSIM values for scale factor 3 are not reported since for d-LCI and d-VPI these values, being equal to infinity, are not comparable with those of the other methods.

Table 3: Average performance results on DIV2k dataset classified (-B) and (-u) in upscaling

	x2			x3			x4		
	PSNR	SSIM	T	PSNR	SSIM	T	PSNR	SSIM	T
DIV2k-T-B									
BIC	32,369	0,944	0,036	29,623	0,899	0,031	28,094	0,865	0,032
SCN	34,336	0,960	14,353	30,924	0,918	30,972	29,170	0,884	17,879
u-LCI	32,969	0,948	0,245	29,967	0,903	0,175	28,381	0,868	0,165
u-VPI	33,003	0,949	5,513	30,013	0,905	4,120	28,419	0,870	3,586
DIV2k-V-B									
BIC	32,411	0,940	0,035	29,647	0,891	0,029	28,108	0,853	0,030
SCN	34,513	0,958	14,822	31,078	0,912	32,872	29,312	0,875	18,855
u-LCI	33,010	0,944	0,252	29,989	0,895	0,197	28,396	0,856	0,152
u-VPI	33,072	0,946	5,796	30,036	0,897	4,416	28,433	0,859	4,450
DIV2k-T-u									
BIC	26,566	0,835	0,035	27,292	0,849	0,025	23,409	0,751	0,023
SCN	26,444	0,831	14,442	27,378	0,853	29,500	27,292	0,849	17,568
u-LCI	26,525	0,834	0,233	27,430	0,853	0,176	23,357	0,749	0,149
u-VPI	26,586	0,836	5,498	27,433	0,854	4,235	23,435	0,752	3,518
DIV2k-V-u									
BIC	26,536	0,820	0,029	27,279	0,836	0,029	23,233	0,726	0,027
SCN	26,412	0,816	14,976	27,368	0,840	32,270	23,074	0,720	18,362
u-LCI	26,496	0,818	0,248	27,418	0,840	0,179	23,180	0,724	0,147
u-VPI	26,557	0,821	5,661	27,421	0,841	4,287	23,262	0,727	3,591

By Table 6 it results that:

- The average performance trend observed in Table 1 is further confirmed. Even for high downscaling factors, d-VPI produces the best results, followed by d-LCI and BIC ;
- As the scale factor increases, the PSNR and SSIM values provided by d-VPI and d-LCI increase too,

while those provided by BIC are almost the same at any scale. Moreover, we observe an increasing gap between d-VPI and both BIC and d-LCI. In fact, comparing d-VPI and BIC, for $s=10$ the PSNR difference ranges from $26.5db$ to $32db$, while it ranges from $38.5db$ to $44.2db$ when $s = 30$. By comparing d-VPI and d-LCI we observe that the gap is much smaller than before but still grows with the scale

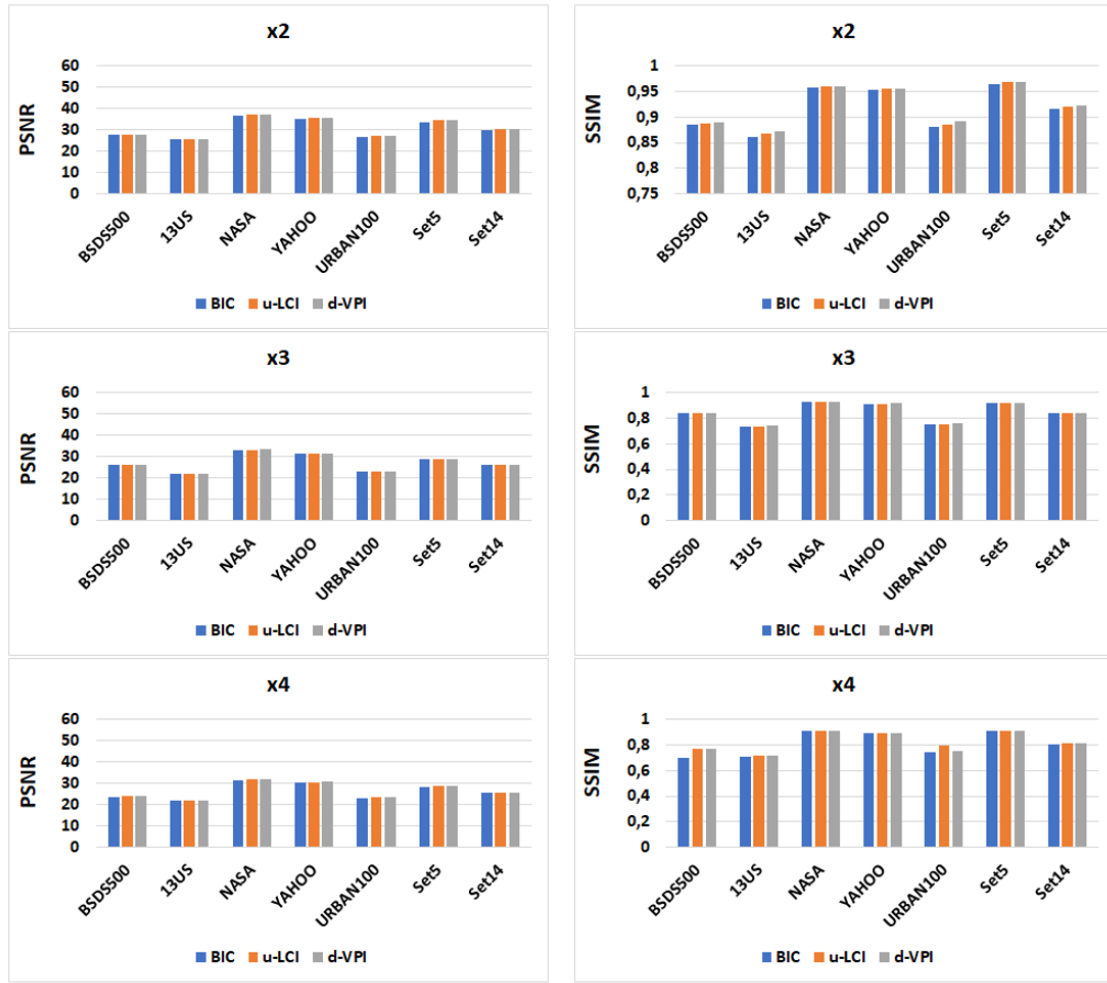


Fig. 12: PSNR and SSIM values for the scale factor 2 (top), at the scale factor 3 (middle) and at the scale factor 4 (bottom) respectively extracted from Table 2.

Table 4: Average performance results on DIV2k classified as difficult (-d) and mild (-m) in upscaling.

	x4				x4		
	PSNR	SSIM	T		PSNR	SSIM	T
DIV2k-T-d				DIV2k-V-d			
BIC	20,056	0,665	0,022	BIC	23,233	0,726	0,024
SCN	19,956	0,649	17,842	SCN	19,824	0,621	18,532
u-LCI	20,010	0,656	0,150	u-LCI	19,876	0,628	0,150
u-VPI	20,138	0,672	3,581	u-VPI	20,012	0,644	3,597
DIV2k-T-m				DIV2k-V-m			
BIC	19,589	0,652	0,023	BIC	23,233	0,726	0,024
SCN	19,475	0,636	17,608	SCN	19,047	0,601	18,496
u-LCI	19,530	0,643	0,151	u-LCI	19,095	0,608	0,150
u-VPI	19,735	0,661	3,592	u-VPI	19,332	0,627	3,645

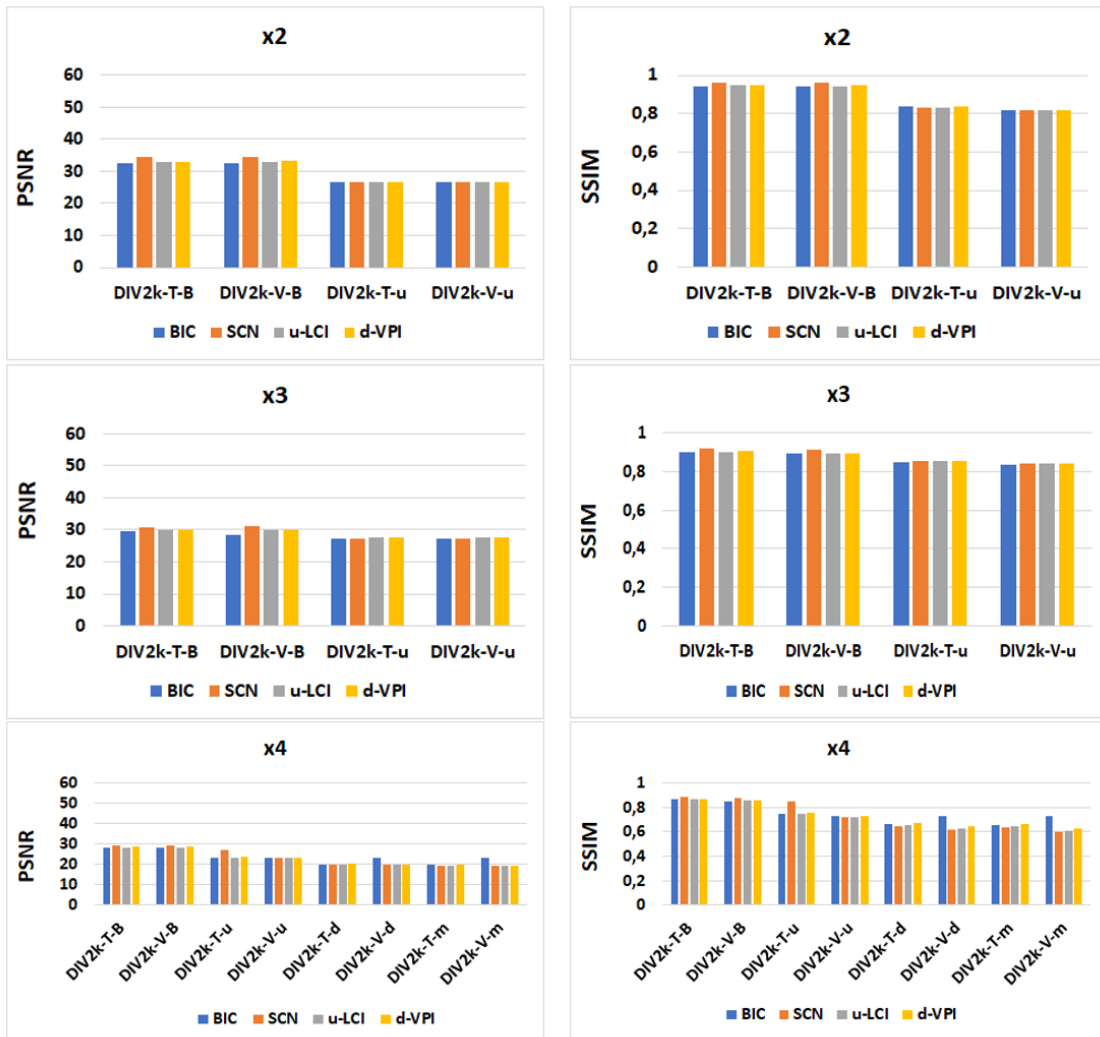


Fig. 13: PSNR and SSIM values for the scale factor 2 (top), at the scale factor 3 (middle) and at the scale factor 4 (bottom) respectively extracted from Table 3.

factor. Indeed, for $s=10$ the difference between the PSNR values of d-VPI and d-LCI varies from $3.7db$ to $9.1db$, while for $s=30$, it ranges from $6.3db$ to $12.2db$.

- c) The values achieved for $s = 15$ and $s = 30$ confirm the advantage of using an odd scale factor, according to Proposition 1.
- d) Due to the adopted optimization procedure (see the previous point 4), also in this case, the CPU time required by d-VPI is bigger than BIC and d-LCI.

6 Conclusions

In this paper, we propose the image scaling method VPI in both downscaling and upscaling directions. It

is the first to employ the sampling of a bivariate de la Vallée-Poussin filtered polynomial. VPI is fully automatic since no input parameters are needed and is a flexible tool as the resized image can be originated specifying the scale factor or the size. No correction step is required to improve the resulting scaled image.

The VPI performance has been evaluated using two commonly adopted quality measures on a wide range of input images characterized by different contents and sizes ranging from small to large scale. The experimental results confirm that VPI has a competitive and satisfactory performance concerning other existing scaling methods as salient details are preserved and/or blurring/artifact effects are, on the whole, largely absent. Further, downscaling VPI has a better performance than

other downscaling methods, achieving very high SSIM and PSNR values. For the special case of odd scale factors, downscaling VPI performance coincides with that of downscaling LCI. Moreover, for this special case, we state a theoretical estimate for MSE. On the other hand, upscaling VPI performance is comparable to other methods with sometimes an equal or slightly lower/upper value of visual quality measures.

Due to the above features, we consider VPI particularly suitable for use in real-world applications. Finally, in future investigations, we believe that there is room to improve it in different directions.

Funding

This research was partially supported by University of Basilicata (local funds) and by GNCS (Gruppo Nazionale di Calcolo Scientifico) of the INDAM (Istituto Nazionale di Alta Matematica).

Code and supplementary materials

The code and the supplementary materials will be openly available at a GitHub link after the publication.

References

- Arcelli, C., Brancati, N., Frucci, M., Ramella, G., Sanniti di Baja, G.: A fully automatic one-scan adaptive zooming algorithm for color images. *Signal Processing* **91** (1), 61-71 (2011)
- Atkinson, P.M.: Downscaling in remote sensing. *International Journal of Applied Earth Observation and Geoinformation*, **22**, 106-114 (2013)
- Bevilacqua, M., Roumy, A., Guillemot, C., Alberi-Morel, M. L.: Low-complexity single-image super-resolution based on nonnegative neighbor embedding. In *Proc. British Machine Vision Conference* (2012)
- Burger, W., Burge, M.J.: *Digital Image Processing An Algorithmic Introduction Using Java*. Springer (2016)
- Bruni, V., Ramella, G., Vitulano, D.: An Adaptive Copy-Move Forgery Detection Using Wavelet Coefficients Multiscale Decay. In *CAIP 2019*, M. Vento, G. Percannella Eds., *Lecture Notes in Computer Science* 11678, part I, pp. 469-480. Springer (2019)
- Bruni V., Ramella G., Vitulano D. : Automatic Perceptual Color Quantization of Dermoscopic Images. In *VIS-APP 2015*, J. Braz et al. Eds., 1, pp. 323-330. Scitepress Science and Technology Publications (2015)
- Capobianco, M.R., Themistoclakis, W.: Interpolating polynomial wavelets on $[-1, 1]$. *Advances in Computational Mathematics*, **23**(4), 353-374 (2004)
- Chaki J., Dey N.: Introduction to Image Color Feature. In: *Image Color Feature Extraction Techniques*. SpringerBriefs in Applied Sciences and Technology. Springer, Singapor (2021)
- Chen, H., Lu, M., Ma, Z., Zhang, X., Xu et al.: Learned Resolution Scaling Powered Gaming-as-a-Service at Scale, *IEEE Transactions on Multimedia*, **23**, 584-596 (2021)
- Chen, G., Zhao H., Pang, C. K., Li, T., Pang, C.: Image Scaling: How Hard Can It Be? *IEEEAccess*, **7** 129452-129465 (2019)
- De Bonis, M.C., Occorsio D., Themistoclakis, W.: Filtered interpolation for solving Prandtl's integro-differential equations, *Numer. Alg.* **88** (2), 679-709 (2021)
- De Bonis, M.C., Occorsio, D., Quadrature methods for integro-differential equations of Prandtl's type in weighted spaces of continuous functions, *Appl. Math. and Comput.* **393**, art. 125721 (2021)
- De Marchi, S., Erb, W., Francomano, E., Marchetti, F., Perracchione, E., Poggiali, D.: Fake Nodes approximation for Magnetic Particle Imaging. In *20th IEEE Mediterranean Electrotechnical Conference, MELECON 2020 - Proceedings*, pp. 434-438 (2020)
- Filbir F., Themistoclakis W.: On the construction of de la Vallée Poussin means for orthogonal polynomials using convolution structures, *Journal of Computational Analysis and Applications*, **6** (4), 297 - 312 (2004)
- Han, D.: Comparison of Commonly Used Image Interpolation Methods. In *Proceedings of the 2nd International Conference on Computer Science and Electronics Engineering*, pp. 1556-1559 (2013)
- Hayat, K.: Multimedia super-resolution via deep learning: A survey. *Digital SignalProcessing*, **81**, 198-217 (2018)
- Huang, J.-B., Singh, A., Ahuja, N.: Single image super-resolution from transformed self-exemplars. In *Proc. CVPR 2015*, pp. 5197-5206 (2015)
- Keys, R. G.: Cubic Convolution Interpolation for Digital Image Processing. *IEEE Trans. on Acoustics, Speech, and Signal Processing*, **29** (6), 1153-1160 (1981)
- Kopf, J., Shamir, A., Peers, P.: Content-adaptive image downscaling. *ACM Transactions on Graphics*, **32** (6), article 173 (2013)
- Li, X., Wu, Y., Zhang, W., Wang, R., Hou, F.: Deep learning methods in real-time image super-resolution: a survey. *Journal of Real-Time Image Processing*, **17**, 1885-1909 (2020)
- Lin, X., Li, J., Wanga, S., Liew, A., Cheng, F., Huang, X.: Recent Advances in Passive Digital Image Security Forensics: A Brief Review, *Engineering* **4**, 29-39 (2018)
- Liu, H., Xie X., Ma, W.Y., Zhang, H.J.: Automatic Browsing of Large Pictures on Mobile Devices. In *11th ACM International Conference on Multimedia*, Berkeley, CA, USA, 2003.
- Liu, J., He, S., Lau, R. W. H.: L_0 Regularized Image Downscaling. *IEEE Trans. Image process.*, **27** (3) (2018)
- Liu, T., Yuan, Z., Sun, J., Wang, J., Zheng, N., Tang, X., Shum, H.-Y.: Learning to detect a salient object, *IEEE Trans. on Patt. Anal. Mach. Intell.* **33** (2), 353-367 (2011).
- Lookingbill, A., Rogers, J., Lieb, D., Curry, J., Thrun, S.: Reverse Optical Flow for Self-Supervised Adaptive Autonomous Robot Navigation. *International Journal of Computer Vision* **74** (3), 287-302 (2007)
- Madhukar B.N., Narendra R.: Lanczos Resampling for the Digital Processing of Remotely Sensed Images., in *Proc. of International Conference on VLSI, Communication, Advanced Devices, Signals & Systems and Networking (VCASAN-2013)*. Chakravarthi V., Shirur Y., Prasad R. (eds) . *Lecture Notes in Electrical Engineering*, vol 258, pp. 403-411. Springer (2013)
- Martin, D., Fowlkes, C., Tal, D., Malik, J.: A database of human segmented natural images and its application to evaluating segmentation algorithms and measuring

- ecological statistics. In Proc. 8th Int. Conf. Computer Vision, vol.2, pp. 416–423 (2001)
28. Mastroianni, G., Russo, M.G., Themistoclakis, W.: The boundedness of the Cauchy singular integral operator in weighted Besov type spaces with uniform norms. *Integral Equations Operator Theory* **42** (1), 57–89 (2002)
 29. Mastroianni G., Themistoclakis, W.: De la Vallée Poussin means and Jackson theorem, *Acta Sci. Math. (Széged)* **74**, 147–170 (2008)
 30. Mastroianni G., Themistoclakis, W.: A numerical method for the generalized airfoil equation based on the de la Vallée Poussin interpolation. *J. Comput. Appl. Math.* **180**, pp.71–105 (2005)
 31. Meijering, E.H.W., Niessen, W.J., Viergever, M.A.: Quantitative evaluation of convolution-based methods for medical image interpolation. *Medical Image Analysis* **5**, 111–126 (2001)
 32. Mittal, H., Pandey, A.C., Saraswat, M. et al. : A comprehensive survey of image segmentation: clustering methods, performance parameters, and benchmark datasets. *Multimed Tools Appl.* (2021)
 33. Neetha C.H., John Moses C., Selvathi D.: Image Interpolation Using Non-adaptive Scaling Algorithms for Multimedia Applications—A Survey, in *Advances in Automation, Signal Processing, Instrumentation, and Control*, Komanapalli V.L.N., Sivakumaran N., Hampannavar S. (eds), *Lecture Notes in Electrical Engineering*, vol 700, Springer, pp. 1509-1516 (2021)
 34. Occorsio D., Ramella G.: Themistoclakis W. Image scaling by Lagrange–Chebyshev Interpolation, [arXiv:2109.03779](https://arxiv.org/abs/2109.03779) (2021).
 35. Occorsio D., Russo M.G.: Numerical methods for Fredholm integral equations on the square. *Appl. Math. and Comput.* **218** (5), 2318–2333 (2011)
 36. Occorsio, D., Themistoclakis, W.: Some remarks on filtered polynomial interpolation at chebyshev nodes, *Dolomites Research Notes on Approximation*, **14**, 68–84 (2021)
 37. Occorsio, D., Themistoclakis, W.: On the filtered polynomial interpolation at Chebyshev nodes, *Applied Numerical Mathematics*, **166**, 272 - 287 (2021)
 38. Occorsio, D., Themistoclakis, W.: Uniform weighted approximation on the square by polynomial interpolation at Chebyshev nodes. *Applied Mathematics and Computation*, **385**, doi=10.1016/j.amc.2020.125457, art. n. 125457 (2020)
 39. Occorsio, D., Themistoclakis, W.: Uniform Weighted Approximation by Multivariate Filtered Polynomials, *Lecture Notes in Computer Science*, 11973, pp. 86 - 100 (2020)
 40. Occorsio, D., Russo, M.G., Themistoclakis, W.: Filtered integration rules for finite Hilbert transform, [arXiv:2109.10634](https://arxiv.org/abs/2109.10634) (2021)
 41. Oztireli, A. C., Gross, M.: Perceptually based downscaling of images, *ACM Trans. Graph.* **34** (4), Article 77, (2015)
 42. Poggiali, D., Cecchin, D., Campi, C., De Marchi, S.: Oversampling errors in multimodal medical imaging are due to the Gibbs effect, *Mathematics* **9** (12), art. number 1348 (2021)
 43. Pratt, W.K.: *Digital Image Processing*. John Wiley & Sons, New York (2001)
 44. Ramella G., Sanniti di Baja G.: Color histogram-based image segmentation. In *Computer Analysis of Images and Patterns – CAIP 2011*, P. Real, D. Diaz-Pernil, H. Molina-Abril, A. Berciano, W. Kropatsch Eds., *Lecture Notes in Computer Science* 6854, Springer, I, pp. 76-83 (2011)
 45. Ramella, G., Sanniti di Baja, G.: Image segmentation based on representative colors and region merging. In *Pattern Recognition*, J. A. Carrasco-Ochoa et al Eds., 611 *Lecture Notes in Computer Science* 7914, Springer, pp. 175-184 (2013)
 46. Ramella G., Sanniti di Baja G.: From color quantization to image segmentation. In Proc. 12th Internat. Conf. Signal Imag. Techn. Internet-Based Syst. - SITIS 2016, K. Yetongnon et al. Eds., *IEEE Computer Society*, pp. 798-804 (2016)
 47. Ramella G.: Evaluation of quality measures for color quantization, *Multimedia Tools and Applications*, DOI: 10.1007/s11042-021-11385-y, 1-35 (2021)
 48. Ramella G., Sanniti di Baja G.: A new technique for color quantization based on histogram analysis and clustering. *Int. J. Patt. Recog. Artif. Intell.* **27** (3), 1-17 (2013)
 49. Ramella G., Sanniti di Baja G.: A new method for color quantization. In Proc. 12th Intern. Conf. Signal Imag. Techn. Internet-Based Syst. - SITIS 2016, K. Yetongnon et al. Eds., *IEEE Computer Society*, pp. 1-6 (2016)
 50. Setlur, V., Takagi, S., Raskar, R., Gleicher, M., Gooch, B.: Automatic image retargeting. In *Proceedings of the 4th international conference on Mobile and ubiquitous multimedia*, pp. 59-68 (2005)
 51. Stentiford, F. W. M., Attention based auto image cropping. In Proc. 5th International Conference on Computer Vision Systems, Bielefeld (2007)
 52. Themistoclakis, W.: Uniform approximation on $[-1, 1]$ via discrete de la Vallée Poussin means, *Numerical Algorithms*, **60** (4), 593 - 612 (2012)
 53. Themistoclakis, W.: Weighted L_1 approximation on $[-1, 1]$ via discrete de la Vallée Poussin mean. *Mathematics and Computers in Simulation*, **147**, 279-292 (2018)
 54. Themistoclakis, W.: Some error bounds for Gauss-Jacobi quadrature rules. *Appl. Numer. Math.* **116**, 286–293 (2017)
 55. Themistoclakis, W., Van Barel, M.: Generalized de la Vallée Poussin approximations on $[-1, 1]$, *Numerical Algorithms*, **75** (1), 1-31 (2017)
 56. Thomee, B., Shamma, D. A., Friedland, G., Elizalde, B., Ni, K., Poland, D., Borth, D., Li, L.-J.: YFCC100M: The new data in multimedia research. *Communications of the ACM* **59** (2), (2016)
 57. Timofte, R., Agustsson, E., Van Gool, L., Yang, M.-H., Zhang, L., et al.: Ntire 2017 challenge on single image super-resolution: Methods and results. In the *IEEE Conference on Computer Vision and Pattern Recognition (CVPR) Workshop*, (2017)
 58. Unser, M., Aldroubi, A., Eden, M.: Fast B-Spline Transforms for Continuous Image Representation and Interpolation. *IEEE Transactions on Pattern Analysis and Machine Intelligence* **13** (3), 277-285 (1991)
 59. Vlašić, T., Ralašić, I., Tafro, A., Seršić, D.: Spline-like Chebyshev polynomial model for compressive imaging, *J. Vis. Commun. Image R.* **66** (2020)
 60. Wang, Z., Liu, D., Yang, J., Han, W., Huang, T.: Deep networks for image super-resolution with sparse prior. *IEEE International Conference on Computer Vision*, (2015)
 61. Wang Z., Bovik A. C., Sheikh H. R., Simoncelli E. P.: Image quality assessment: from error visibility to structural similarity. *IEEE Trans. Imag. Proc.* 2004, **13** (4), 600-612 (2004)

62. Weber, N., Waechter, M., Amend, S. C., Guthe, S., Goesele, M., Rapid, Detail-Preserving Image Down-scaling, *ACM Trans. Graph.*, **35** (6), article number 205 (2016)
63. Xiao, Q., Chen, Y., Shen, C., Chen, Y., Li, K.: Seeing is not believing: Camouflage attacks on image scaling algorithms. In *Proc. of the 28th USENIX Security Symposium*, pp. 443 - 460 (2019)
64. Yang, J., Wright, J., Huang, T. et al.: Image super-resolution via sparse representation. *IEEE Trans. Image Process.*, **19** (11) (2010)
65. Yang, W., Zhang, X., Tian, Y., Wang, W., Xue, J.-H., Liao, Q.: Deep Learning for Single Image Super-Resolution: A Brief Review. *IEEE Trans. on Multimedia* **21** (12) (2019)
66. Yao T., Luo Y., Chen Y., Yang D., Zhao L.: Single-Image Super-Resolution: A Survey. In *Communications, Signal Processing, and Systems. CSPA 2018*. Liang Q., Liu X., Na Z., Wang W., Mu J., Zhang B. (eds), *Lecture Notes in Electrical Engineering*, vol 516, Springer, pp. 119-125 (2020)
67. Zeyde, R., Elad, M., Protter, M.: On single image scale-up using sparse-representations. In *Proc. International Conference on Curves and Surfaces*, pp. 711–730 (2010)
68. Zhang, M., Zhang, L., Sun, Y., Feng, L., Ma, W.: Auto cropping for digital photographs. In *2005 IEEE International Conference on Multimedia and Expo*, pp. 4 (2005)
69. Zhou, D.-X.: Theory of deep convolutional neural networks: Downsampling. *Neural Networks* **124**, 319–327 (2020)
70. <https://it.mathworks.com/help/vision/ref/psnr.html>
71. www2.eecs.berkeley.edu/Research/Projects/CS/vision/bsds/
72. <https://www.cl.cam.ac.uk/aco41/Files/Sig15UserStudyImages.html>
73. National Aeronautics and Space Administration, 2016. NASA image gallery. <https://www.nasa.gov/multimedia/imagegallery/index.html>
74. <https://www.gcc.tu-darmstadt.de/home/proj/dpid/index.en.jsp>
75. <https://data.vision.ee.ethz.ch/cvl/DIV2K/>

Table 5: Pointwise performance results on 10 images randomly selected from 13US and NASA datasets (oom means "out of memory" and n.c. means "not computed")

	:2		:3		:4		δ
	PSNR	SSIM	PSNR	SSIM	PSNR	SSIM	
US1 (300 × 400)							
BIC	39,579	0,995	39,922	0,996	39,847	0,996	0.67%
DPID	42,322	0,997	42,149	0,997	41,524	0,997	-1.92%
L ₀	29,555	0,949	34,404	0,971	36,752	0,978	19.58%
d-LCI	55,261	0,999	Inf	1,000	57,473	1,000	3.85%
d-VPI	56,339	0,999	Inf	1,000	61,232	1,000	7.99%
US3 (300 × 400)							
BIC	44,639	0,999	45,114	0,999	45,008	0,999	0.82%
DPID	46,589	0,999	46,478	0,999	45,913	0,999	-1.47%
L ₀	32,637	0,986	36,637	0,992	38,134	0,994	14.41%
d-LCI	55,681	1,000	Inf	1,000	57,807	1,000	3.68%
d-VPI	57,110	1,000	Inf	1,000	62,078	1,000	8.00%
US7 (273 × 400)							
BIC	41,487	0,994	41,832	0,995	41,766	0,995	0.67%
DPID	43,951	0,997	44,446	0,997	43,808	0,997	-0.33%
L ₀	30,163	0,942	33,386	0,949	34,642	0,953	12.93%
d-LCI	55,747	1,000	Inf	1,000	57,145	1,000	2.45%
d-VPI	57,042	1,000	Inf	1,000	61,811	1,000	7.72%
US10 (400 × 307)							
BIC	36,212	0,992	36,522	0,992	36,459	0,992	0.68%
DPID	39,989	0,997	40,239	0,997	39,483	0,997	-1.28%
L ₀	27,383	0,962	32,701	0,984	35,418	0,988	22.69%
d-LCI	54,826	1,000	Inf	1,000	57,138	1,000	4.05%
d-VPI	55,885	1,000	Inf	1,000	60,479	1,000	7.60%
US13 (310 × 400)							
BIC	39,187	0,995	39,522	0,996	39,457	0,996	0.68%
DPID	41,958	0,998	42,340	0,998	41,739	0,998	-0.52%
L ₀	28,563	0,970	33,096	0,982	35,831	0,987	20.28%
d-LCI	55,158	1,000	Inf	1,000	57,295	1,000	3.73%
d-VPI	56,312	1,000	Inf	1,000	61,332	1,000	8.18%
N3 (2048 × 1536)							
BIC	47,602	0,996	48,281	0,997	48,184	0,997	1.21%
DPID	50,057	0,998	50,135	0,998	49,558	0,998	-1.01%
L ₀	37,159	0,956	40,219	0,968	oom	oom	n.c.
d-LCI	55,631	0,998	Inf	1,000	59,524	0,999	6.54%
d-VPI	57,929	0,999	Inf	1,000	64,684	1,000	10.44%
N5 (2701 × 3665)							
BIC	45,290	0,998	45,696	0,999	45,623	0,999	0.73%
DPID	45,932	0,999	45,775	0,999	45,207	0,999	-1.60%
L ₀	33,417	0,987	36,487	0,991	oom	oom	n.c.
d-LCI	55,315	1,000	Inf	1,000	56,226	1,000	1.62%
d-VPI	56,349	1,000	Inf	1,000	60,806	1,000	7.33%
N9 (5430 × 3520)							
BIC	47,869	0,998	48,428	0,999	48,338	0,999	0.97%
DPID	49,538	0,999	49,519	0,999	48,901	0,999	-1.30%
L ₀	36,538	0,982	38,550	0,986	oom	oom	n.c.
d-LCI	55,861	1,000	Inf	1,000	57,338	1,000	2.58%
d-VPI	57,286	1,000	Inf	1,000	62,618	1,000	8.50%
N14 (3456 × 5184)							
BIC	54,239	0,999	57,088	1,000	57,009	1,000	4.86%
DPID	56,981	0,999	56,641	0,999	56,697	1,000	-0.50%
L ₀	44,505	0,990	46,565	0,992	oom	oom	n.c.
d-LCI	55,304	0,998	Inf	1,000	62,202	1,000	11.09
d-VPI	60,405	1,000	Inf	1,000	73,799	1,000	18.15%
N16 (5501 × 3095)							
BIC	58,052	0,999	63,214	1,000	62,604	1,000	7.27%
DPID	57,760	0,999	57,314	0,999	56,908	0,999	-1.50%
L ₀	43,430	0,988	46,189	0,992	oom	oom	n.c.
d-LCI	56,784	0,999	Inf	1,000	63,961	1,000	11.22%
d-VPI	63,024	1,000	Inf	1,000	73,779	1,000	14.58 %

Table 6: Performance results on 13US dataset for high downsampling.

	:10			:15			:30		
	PSNR	SSIM	T	PSNR	SSIM	T	PSNR	SSIM	T
US1 (300 × 400)									
BIC	39,876	0,996	0,056	39,879	0,996	0,122	39,880	0,996	0,408
d-LCI	61,677	1,000	0,415	Inf	1,000	0,709	71,511	1,000	2,989
d-VPI	68,633	1,000	5,567	Inf	1,000	11,347	79,946	1,000	40,374
US2 (400 × 300)									
BIC	34,612	0,987	0,063	34,612	0,987	0,107	34,612	0,987	0,401
d-LCI	57,928	1,000	0,472	Inf	1,000	0,808	66,737	1,000	3,562
d-VPI	64,921	1,000	6,461	Inf	1,000	12,726	76,346	1,000	44,041
US3 (300 × 400)									
BIC	45,074	0,999	0,063	45,073	0,999	0,115	45,076	0,999	0,397
d-LCI	63,364	1,000	0,415	Inf	1,000	0,725	75,558	1,000	2,950
d-VPI	71,607	1,000	5,595	Inf	1,000	10,872	87,783	1,000	37,452
US4 (300 × 400)									
BIC	41,920	0,996	0,063	41,910	0,996	0,098	41,916	0,996	0,407
d-LCI	62,675	1,000	0,403	Inf	1,000	0,688	72,795	1,000	3,487
d-VPI	70,964	1,000	5,509	Inf	1,000	11,017	81,933	1,000	36,993
US5 (400 × 300)									
BIC	31,625	0,979	0,053	31,625	0,979	0,102	31,626	0,979	0,378
d-LCI	56,747	1,000	0,474	Inf	1,000	0,757	64,521	1,000	3,355
d-VPI	63,557	1,000	6,211	Inf	1,000	12,521	75,869	1,000	43,893
US6 (300 × 400)									
BIC	30,966	0,978	0,066	30,967	0,978	0,099	30,966	0,978	0,372
d-LCI	55,913	1,000	0,463	Inf	1,000	0,682	63,481	1,000	3,123
d-VPI	61,061	1,000	5,563	Inf	1,000	11,149	70,868	1,000	38,515
US7 (273 × 400)									
BIC	41,791	0,995	0,059	41,792	0,995	0,193	41,799	0,995	0,431
d-LCI	61,405	1,000	0,410	Inf	1,000	0,624	73,110	1,000	2,713
d-VPI	70,568	1,000	4,936	Inf	1,000	9,596	80,805	1,000	34,353
US8 (241 × 400)									
BIC	33,114	0,989	0,057	33,115	0,989	0,081	33,116	0,989	0,323
d-LCI	59,209	1,000	0,306	Inf	1,000	0,525	68,362	1,000	2,544
d-VPI	65,225	1,000	4,347	Inf	1,000	8,572	76,068	1,000	28,882
US9 (322 × 400)									
BIC	29,508	0,984	0,065	29,507	0,984	0,126	29,508	0,984	0,412
d-LCI	55,903	1,000	0,492	Inf	1,000	0,721	63,094	1,000	3,129
d-VPI	60,512	1,000	1,061	Inf	1,000	12,155	71,216	1,000	41,401
US10 (400 × 307)									
BIC	36,476	0,992	0,065	36,474	0,992	0,108	36,476	0,992	0,412
d-LCI	59,817	1,000	0,509	Inf	1,000	0,796	68,672	1,000	3,486
d-VPI	67,500	1,000	6,698	Inf	1,000	13,679	78,454	1,000	47,070
US11 (400 × 241)									
BIC	35,794	0,992	0,039	35,794	0,995	0,087	35,792	0,995	0,310
d-LCI	60,143	1,000	0,368	Inf	1,000	0,559	67,993	1,000	2,721
d-VPI	63,847	1,000	5,272	Inf	1,000	10,766	74,335	1,000	36,261
US12 (400 × 266)									
BIC	36,958	0,993	0,059	36,957	0,993	0,084	36,957	0,993	0,358
d-LCI	59,118	1,000	0,413	Inf	1,000	0,685	68,729	1,000	3,068
d-VPI	66,730	1,000	5,580	Inf	1,000	11,265	76,877	1,000	38,968
US13 (310 × 400)									
BIC	39,473	0,996	0,063	39,475	0,996	0,116	39,477	0,996	0,413
d-LCI	61,742	1,000	0,443	Inf	1,000	0,725	71,606	1,000	3,260
d-VPI	69,937	1,000	5,859	Inf	1,000	11,668	80,200	1,000	39,543